Accepted Manuscript

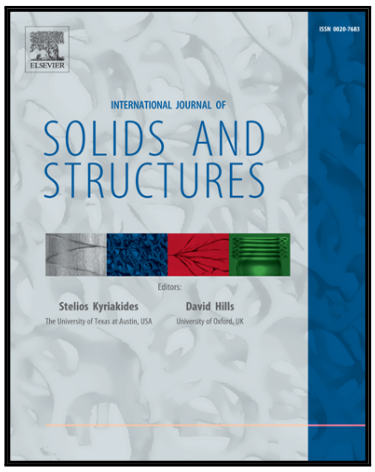

Failure Parameter Identification and Validation for a Dual-Phase 780 Steel Sheet

D. Anderson , C. Butcher , N. Pathak , M.J. Worswick

PII: S0020-7683(17)30284-6
DOI: 10.1016/j.ijsolstr.2017.06.018
Reference: SAS 9625

To appear in: *International Journal of Solids and Structures*

Received date: 5 January 2017
Revised date: 16 June 2017
Accepted date: 17 June 2017

Please cite this article as: D. Anderson , C. Butcher , N. Pathak , M.J. Worswick , Failure Parameter Identification and Validation for a Dual-Phase 780 Steel Sheet , *International Journal of Solids and Structures* (2017), doi: 10.1016/j.ijsolstr.2017.06.018

Failure Parameter Identification and Validation for a Dual-Phase 780 Steel Sheet

D. Anderson[1,2], C. Butcher*[1], N. Pathak[1], M.J. Worswick[1]

[1]Mechanical and Mechatronics Engineering, University of Waterloo, 200 University Ave. W., Waterloo, Ontario, Canada, N2L 3G1

[2]Current affiliation: Novelis, Inc., 1950 Vaughn Rd, Kennesaw, Georgia, United States, 30144

david.anderson@novelis.com, cbutcher@uwaterloo.ca, n3pathak@uwaterloo.ca, worswick@lagavulin.uwaterloo.ca

*Corresponding author, Tel.: +1-519-888-4567 x. 31795

Abstract

A hybrid experimental-numerical procedure was implemented to determine the failure surface of a dual-phase 780 steel sheet as a function of the effective plastic strain, triaxiality, and Lode parameter using butterfly specimens with in situ digital image correlation strain measurement and supporting finite element calculations. A butterfly-type test specimen was employed to experimentally obtain stress states ranging from simple shear to plane strain tension including mixed tensile and shear loading. The numerically-derived failure surface was implemented into the phenomenological GISSMO damage model in the commercial finite element code LS-DYNA and the accuracy of the failure surface was determined using finite element predictions of the characterization experiments. A series of independent validation experiments related to sheet metal forming were performed including a hole tension test, a conical and flat punch hole expansion test, and a hemispherical punch test. The finite element models utilizing the damage model were able to accurately reproduce the load-displacement and surface strains of the sheet material for both the characterization and validation experiments. Prediction of the failure orientation and location compared favourably to each of the validation tests.

Keywords: damage; fracture; dual-phase 780 steel, butterfly specimen, sheet metal forming, GISSMO, failure prediction

1.0 Introduction

Optimized mechanical design using lightweight construction methods has become a high priority in the automotive industry as pressure mounts to reduce green-house gas emissions and improve fuel economy while maintaining (or improving) performance and safety. It has been shown that a 10% reduction in automotive mass yields a 6% improvement in fuel economy [1]. Additionally, the U.S. Department of Energy [2] has estimated that current automotive mass could be reduced by up to 50%. A key contribution to achieving this mass reduction will be the implementation of lower density and/or higher strength materials in place of commonly used lower strength steel alloys within automotive structural components and closure panels. However, the performance of these materials must be investigated to support simulations of their formability during manufacturing and in-service performance (crashworthiness); as such, the accurate prediction of damage and failure has become a key requirement within the automotive design process. One such alloy is dual-phase (DP) 780 steel. Several publications [3, 4, 5] have studied the performance of this material, including the work of Anderson *et al.* [6] who showed that, under uniaxial conditions, the material displays a weak dependence on strain rate until strain rates exceed approximately $0.1s^{-1}$. They also observed strain rate dependent failure loci that shifted towards higher failure strains in notched tensile specimens as the strain rate was increased.

The forming history of automotive body structures from flat sheet into final components affects the in-service and crashworthiness performance; therefore, accurate prediction of damage accumulation and failure of these components is of great interest. Failure due to localized necking during forming is commonly predicted using strain- [7, 8] or stress-based [9, 10] forming limit diagrams (FLD). Failure due to fracture during crashworthiness simulations was often predicted with simple criteria owing to the size and complexity of crash simulations; however, more complex criteria are being introduced as computing power increases, improved accuracy is desired, and damage/failure models are refined. FLD strategies are useful to predict necking of sheet metal components; however, they are not capable of predicting the predominant shear failure at sheared edges of advanced high strength steels (AHSS) [11, 12], which is inconvenient as many automotive panels are fabricated using punching/shearing with subsequent edge stretching techniques. Strain-to-failure criteria are simple to implement; however, they do

not account for the varied strain path and stress state history throughout a component. Although these methods can be effective, they are not sufficiently accurate. As such, new holistic models have been implemented that can be used to track damage accumulation and predict failure through forming with subsequent crashworthiness operations. A key concept to these models is that they are stress-state dependent, in which failure strain is a function of stress triaxiality, η, and normalized Lode angle parameter, $\bar{\theta}$, which are defined as:

$$\eta = \frac{\sigma_m}{\bar{\sigma}}, \tag{1}$$

$$\bar{\theta} = 1 - \frac{2}{\pi}\cos^{-1}\left[\frac{27}{2}\frac{J_3}{\bar{\sigma}^3}\right] \tag{2}$$

where σ_m is the mean stress, $\bar{\sigma}$ is the equivalent stress, and $J_3 = \sigma_1'\sigma_2'\sigma_3'$ with $\sigma_{1,2,3}'$ equal to the principal deviatoric stresses.

A rigorous analysis of sheared edges of AHSS (specifically DP600, DP780, and DP980) performed by Wu *et al.* [13] demonstrated that the martensite and ferrite phases common to dual-phase steels encourage many sub-cracks to form during the shearing process. These sub-cracks, in conjunction with the reduced ductility of AHSS compared to conventional steels, results in a propensity for shear failure as opposed to ductile failure caused by thinning during automotive panel stamping. Consequently, panels can fracture prior to reaching a forming limit and, as such, different failure prediction models incorporating shear failure are necessary for AHSS. The damage observed by Wu *et al.* in the shear zone of DP steels seems to favour a micromechanical damage evolution model, such as that proposed by Gurson [14] and later expanded by Tvergaard and Needleman [15]. The Gurson-Tvergarrd-Needleman (GTN) model accounts for material degradation by accounting for the nucleation and growth of spherical micro-voids. The GTN model has been shown to work well at high triaxial stress states as shown by Besson *et al.* [16]; however, the GTN model does not account for shear localization of inter-void ligaments leading to poor predictions for low and negative stress triaxialties. Xue [17] and Nahshon and Hutchinson [18] have developed improvements to the GTN model to account for shear localization that were shown by Reis *et al.* [19] to dramatically improve the predictive behaviour under shear loading. Similar work by Butcher *et al.* [20] has shown that the GTN model

modified to account for void shape and shear localization was able to predict the burst pressure, formability, and failure location during tube hydroforming, which encompasses a range of low and high triaxialities. Despite the recent advancements of the GTN model it can be computationally expensive and difficult to implement as many different tests are required to determine the model parameters, with Khan and Liu [21] suggesting that at least 10 GTN material constants are required which are very difficult to calibrate due to strong coupling and the need for detailed microstructural measurements.

Recent industrial failure modeling developments have shifted away from coupled micromechanical damage models to uncoupled empirical and phenomenological damage models. These simplified, uncoupled, models tend to require fewer material constants and can be calibrated with experimental data points. Johnson and Cook [22] developed an empirical model of ductile fracture accounting for strain, strain rate, temperature, and pressure effects and although this model has proven popular for problems involving ductile fracture it is ill-suited to situations where low triaxial conditions exist. Bao and Wierzbicki [23] improved on previous empirical models by formulating three equations that could be fit to experimental failure data to cover the range of negative, low, and high triaxialities. This effort was important as it was one of the first works to show that failure strain was not a monotonically increasing quantity as triaxiality decreased. However, this model did not account for the Lode parameter which was shown by Xue [24] to be an important quantity for failure prediction. Xue proposed a model that incorporated the Lode parameter and demonstrated good predictive success. Lou *et al.* [25] and Lou and Huh [26] also developed a triaxiality- and Lode-dependent failure model based on damage accumulation induced by void nucleation, growth, and shear coalescence of voids and was shown to be effective at predicting failure. Arguably the oldest failure criteria is the maximum shear stress model based on the work of Coulomb [27] and Tresca [28], which was shown by Wierzbicki *et al.* [29] to be remarkably effective at predicting failure. Bai and Wierzbicki [30] developed a modified Mohr-Coulomb failure model accounting for triaxiality and Lode parameter that was shown to be effective and was later expanded by Mohr and Marcadet [31] by incorporating the Hosford [32] flow potential to eliminate the physical inconsistency between stress-based plasticity and strain-based fracture models.

Traditionally, many different specimen geometries have been used to characterize the failure loci of metals. Bao and Wierzbicki [23] used cylindrical and notched cylindrical specimens in compression, smooth and notched round bars in tension, as well as in-plane shear and hole tension specimens to characterize a 2024-T351 aluminum alloy. Bai and Wierzbicki [33] expanded on this data set with flat-grooved specimens to determine the performance of the aluminum in plane strain. Kofiani *et al.* [34] used central hole flat tension and flat notched tension specimens, hemispherical punch tests, round notched specimens, and butterfly specimens loaded in shear and plane strain tension to characterize the failure of an X100 grade pipeline steel. Gruben *et al.* [35] used tension, plane strain, in-plane shear, and modified Arcan specimens to characterize the failure of a DP600 steel sheet.

As the literature has demonstrated, there are a wide variety of specimen geometries available to assess the failure performance of metallic materials. Some of these geometries are not applicable to sheet materials used in automotive stamping processes due to thickness requirements to fabricate the specimens. Recently, a butterfly-shaped geometry has been championed by Wierzbicki *et al.* [36] and Mohr and Henn [37] to determine the plane stress failure locus of sheet metals using a single geometry. Additional work by Dunand and Mohr [38] has led to an optimized design of this butterfly-shaped geometry. This geometry is appealing as it enables many stress states to be tested with only a single geometry; therefore, less time is required manufacturing and preparing several different geometries. However, the geometry is more complex to machine and requires a sophisticated loading apparatus. Moreover, quantities of interest (such as triaxiality and Lode parameter) cannot be directly measured necessitating a hybrid experimental-numerical procedure. Nevertheless, the geometry has proven powerful in the determination of plane stress failure loci of sheet material.

The purpose of the current work is to determine the failure surface of a DP780 steel sheet, pair it with a damage model, and independently validate failure parameters against common material tests. The failure surface was fit to the model proposed by Lou et al. [25] and was paired with the GISSMO [39, 40] damage model. Although previous work [12, 41] has calibrated damage models for DP780, a literature review has not revealed published work detailing the methods to calibrate DP780 solely using butterfly specimens. An emphasis is placed upon evaluating the

calibrated damage model using several independent tests common to sheet metal to forming. This step is critical to avoid a "closed-loop validation" where the failure model is only applied to its calibration tests and naturally provides good failure predictions. The failure surface data was determined using a combination of experimental data and finite element models; the methods, procedures, and results will be presented along with verification and validation of the parameters.

2.0 Damage and Failure Models

2.1 GISSMO damage model

The Generalized Incremental Stress State damage MOdel (GISSMO), developed by Neukamm *et al.* [39, 40] and later expanded by Basaran *et al.* [42], is a phenomenological formulation for ductile damage that accounts for material instability, softening, and failure. As typical with MMC damage models, the term "damage" is used in a broad sense that accounts for all types of microstructural damage and does not have a strong physical foundation with damage that can be quantified from microstructural measurements. It can be alternatively viewed as a fracture metric or "failure tracker" where $D = 0$ corresponds to an undeformed material while $D = 1$ indicates failure. Damage accumulation is based on an incremental formulation found from [43]:

$$\Delta D = \frac{n}{\bar{\varepsilon}_f} D^{\left(1-\frac{1}{n}\right)} \Delta\bar{\varepsilon}_p, \tag{3}$$

where D is the damage value, n is the damage exponent, $\bar{\varepsilon}_f$ is the equivalent plastic failure strain, and $\Delta\bar{\varepsilon}_p$ is the equivalent plastic strain increment. D accumulates in each element during deformation and the element is deleted when $D = 1$. An initial value of $D = 10^{-20}$ is assigned to all elements. $\bar{\varepsilon}_f$ is a function of triaxiality and Lode parameter; therefore, several tests with varying specimen geometry are required to create an appropriate failure locus. The specimen geometry and test procedures used to determine a failure surface of DP780 steel sheet will be discussed below in Section 3.0 of the present work. The damage exponent was assumed as $n = 2$ in accordance with suggestions provided by Xue [44].

Material instability was determined according to [43]:

$$\Delta F = \frac{n}{\bar{\varepsilon}_{p,loc}} F^{\left(1-\frac{1}{n}\right)} \Delta\bar{\varepsilon}_p, \tag{4}$$

where F is the instability measure, and $\bar{\varepsilon}_{p,loc}$ is the triaxiality-dependent equivalent plastic instability strain and, in the current work, was obtained from an FLD of the same lot of DP780 sheet, which was determined by Bardelcik *et al.* [45]. Similar to the *D* parameter, the instability measure, *F*, is a tracking variable that is used to integrate an FLD for non-linear loading where *F* = 0 corresponds to an undeformed material whereas *F* = 1, corresponds to the onset of localization based on reaching the equivalent strain from the converted FLD. The major and minor strains of the FLD (Figure 1a) were converted to equivalent plastic strain and triaxiality based on the work of Müschenborn and Sonne [46] (Figure 1b), assuming linear strain paths and plane stress conditions. Assuming the DP780 to be isotropic, the von Mises equivalent plastic strain, $\bar{\varepsilon}_p$, is found from

$$\bar{\varepsilon}_p = \frac{2}{\sqrt{3}} \sqrt{\varepsilon_1^2 + \varepsilon_2^2 + \varepsilon_1 \varepsilon_2}, \tag{5}$$

where $\varepsilon_{1,2}$ are the major and minor strains. The ratio of principal strain increments,

$$\rho = \frac{d\varepsilon_2}{d\varepsilon_1}, \tag{6}$$

is used to calculate the ratio of principal stresses ,

$$\beta = \frac{\sigma_2}{\sigma_1} = \frac{1 + 2\rho}{2 + \rho}. \tag{7}$$

Finally, triaxiality can be calculated based on the principal stress ratio as

$$\eta = \frac{\beta + 1}{3\sqrt{\beta^2 - \beta + 1}}. \tag{8}$$

It is important to note that the triaxiality computed in Eq. (8) is for coaxial proportional loading conditions where the principal stress and strain directions remain aligned. For example, a triaxiailty of zero in Eq. (8) corresponds to pure shear whereas the experimental shear tests of sheet materials in torsion or in-plane shear provides simple shear loading condition that is only approximately coaxial at low strain levels.

The instability factor, F, accumulates in each element during deformation and when $F = 1$ the current value of D is stored as the critical damage value D_{crit}. Material softening due to void nucleation and growth is approximated by reducing the element stress according to [43]:

$$\sigma = \tilde{\sigma}\left[1 - \left(\frac{D - D_{crit}}{1 - D_{crit}}\right)^f\right], \tag{9}$$

where σ is the reduced stress, $\tilde{\sigma}$ is the current stress, and f is a fading exponent that is adjusted to control the rate of material softening. For the present work $f = 4$ was found to produce the best results.

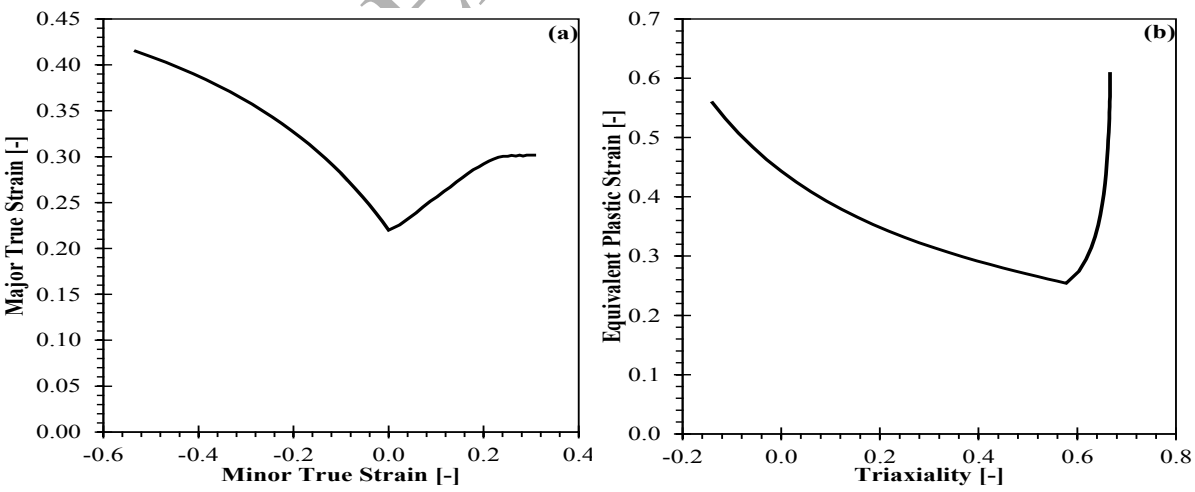

Figure 1 – DP780 forming limit diagrams [45]. a) traditional strain-based diagram, b) transformed into equivalent plastic strain versus triaxiality.

2.2 Failure Surface Model

The failure surface model developed by Lou and Huh [26] was implemented in the present work to provide the GISSMO model with a failure surface in equivalent plastic strain, triaxiality and normalized Lode space. The failure surface is defined by:

$$\left(\frac{2}{\sqrt{L^2+3}}\right)^{C_1}\left(\frac{\langle 1+3\eta\rangle}{2}\right)^{C_2}\bar{\varepsilon}_f = C_3, \tag{10}$$

where $C_{1,2,3}$ are fitting parameters, $\langle\ \ \rangle$ is the Macaulay bracket, and L is the Lode parameter classically defined by [47]:

$$L = \frac{2\sigma_2 - \sigma_1 - \sigma_3}{\sigma_1 - \sigma_3} = \frac{3(\sigma_2 - \sigma_m)}{\sigma_1 - \sigma_3}, \tag{11}$$

and is related to the normalized Lode parameter, $\bar{\theta}$, according to [26]:

$$\sin\left(\frac{\pi\bar{\theta}}{6}\right) = -\frac{L}{\sqrt{L^2+3}}. \tag{12}$$

3.0 Experimental Methods

1.56mm DP780 cold-rolled hot-dip galvanized sheet manufactured by Dofasco Inc. (now ArcelorMittal Dofasco Inc.) was considered in this investigation. The in-plane uniaxial tensile response of the material was determined using sub-size ASTM E8 [48] specimens with a gage length of 25 mm. Anisotropy of the sheet was determined by testing specimens aligned with the rolling, diagonal, and transverse directions. Three repeat tests were acquired for each direction. An Instron model 1331 servo-hydraulic test machine operating in displacement control was used to test the uniaxial samples at a nominal strain rate of $0.001s^{-1}$. Three-dimensional digital image correlation (DIC) was used to determine specimen strain. A three-dimensional DIC system, consisting of a pair of cameras operating in stereo, was chosen to measure strains in the necked region of the specimens up to failure permitting a measure of the true strain in the specimen. A

two-dimensional DIC system, consisting of a single camera, could have been used; however, the out-of-plane motion of the necking material could introduce strain measurement inaccuracies [49]. A subset size of 25, step size of 7, and strain filter size of 13 pixels was used in the DIC software to calculate strains.

The failure surface of the sheet material was determined using the butterfly specimens optimized by Dunand and Mohr [38]. The butterfly specimen used in the present work is shown in Figure 2. The top and bottom of the sheet was symmetrically machined away in the deformation region a total of 0.5mm from each surface leaving an approximately 0.56 mm thick section. A 3.2 mm diameter flat corner radius end mill was used to prevent a sharp corner from developing in the flat-to-radius transition. A special fixture was used to support the butterfly specimen to prevent bending during machining. The machined surface was smoothed and polished with 2000 SiC grit wet sandpaper to remove potential stress raisers left behind by the machining tools.

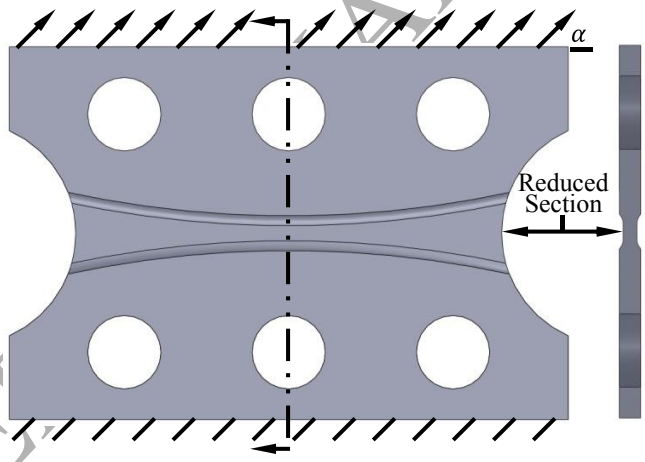

Figure 2 - Butterfly specimen geometry.

A custom fixture, inspired by the work of Wierzbicki *et al.* [36], for testing the butterfly specimens was mounted in a servo-hydraulic test frame as shown in Figure 3. The hydraulic cylinder was operated in displacement control by a custom LabVIEW program interfaced with an MTS FlexTest SE controller. The fixture of Wierzbicki *et al.* [36] was operated in load-control that used a second actuator that would likely provide better control over the stress state. A crosshead speed of 0.05mm/s was used for all of the butterfly tests. Displacement of the

moveable grip was measured with a linear variable differential transformer (LVDT) mounted to the top of the fixture. Vertical loads were measured with a load cell mounted to the hydraulic cylinder. Horizontal reaction loads were measured with a pair of load cells mounted to the top and bottom plates of the fixture. The central section of the fixture was designed to rotate in 5° increments permitting a broad set of stress states from shear to plane strain tension to be achieved. A torque wrench was used to tighten the specimen bolts to ensure consistency between tests. Two sets of fiducial markers, labeled as 1 and 2 in Figure 3, were placed on the fixed and moving grips to permit tracking of the displacements and rotations so that the boundary conditions in the finite-element models can be accurately captured.

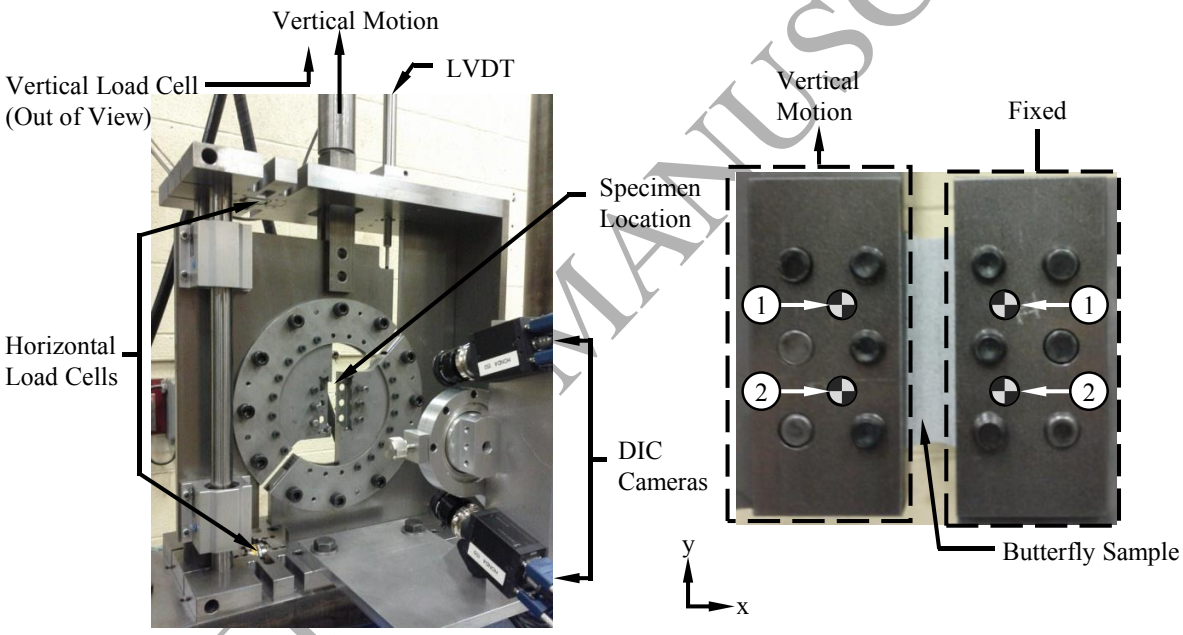

Figure 3 - Butterfly test fixture installed at the University of Waterloo.

According to Mohr and Henn [37] the general stress state obtained in the butterfly specimen corresponds to simple shear with a plane strain extension. Using this assumption, the triaxiality, η, in the butterfly specimen can be approximated according to:

$$\eta = \frac{sign(u)}{\sqrt{3}} \sqrt{\frac{1}{1 + \frac{1}{4\tan^2 \alpha}}}, \tag{13}$$

where $sign(u)$ is +1 for tensile loading and -1 for compressive loading, and α is the loading angle shown in Figure 2. Based on Equation (13) a loading angle of 0° produces a triaxiality of 0 corresponding to a state of simple shear stress while a loading angle of 90° produces a triaxiality of $1/\sqrt{3}$ corresponding to a state of plane strain tension. In the present work, butterfly specimens were tested in tension ($sign(u) = +1$) at 0°, 5°, 10°, 20°, 40°, 60°, and 90° with three tests per orientation producing approximate triaxialities of 0.00, 0.10, 0.19, 0.34, 0.49, 0.55, and 0.57. It is desirable to obtain failure parameters in the compression region ($sign(u) = -1$); however, the central machined section of the specimen was too thin, resulting in buckling under compression. Stereoscopic DIC was also used to measure the surface strains of the butterfly specimens. A custom camera mount was integrated into the fixture to permit rotation of the cameras as the central grip section is rotated and was required to maintain full view of the specimen deformation.

4.0 Experimental Results

Figure 4a displays the uniaxial tensile engineering stress-strain response for the rolling, diagonal, and transverse directions with three tests shown per condition, while Figure 4b is the average response of the three directions. As Figure 4a shows there was good repeatability in the tests with the scatter in the measured data prior to UTS being less than 1% for each direction. Figure 4b demonstrates that there was minimal difference in the stress-strain response with respect to sheet direction, with the variation being less than 4% between the average minimum and average maximum stresses at an engineering strain of 10%. Lankford coefficients were determined for the three directions and were found to be 0.72, 0.98, and 0.92 for the rolling, diagonal, and transverse directions respectively, resulting in an in-plane average value of 0.90. The uniaxial tension results indicate that anisotropy was minimal for the material under investigation; therefore, isotropic conditions were assumed for the remainder of the present work.

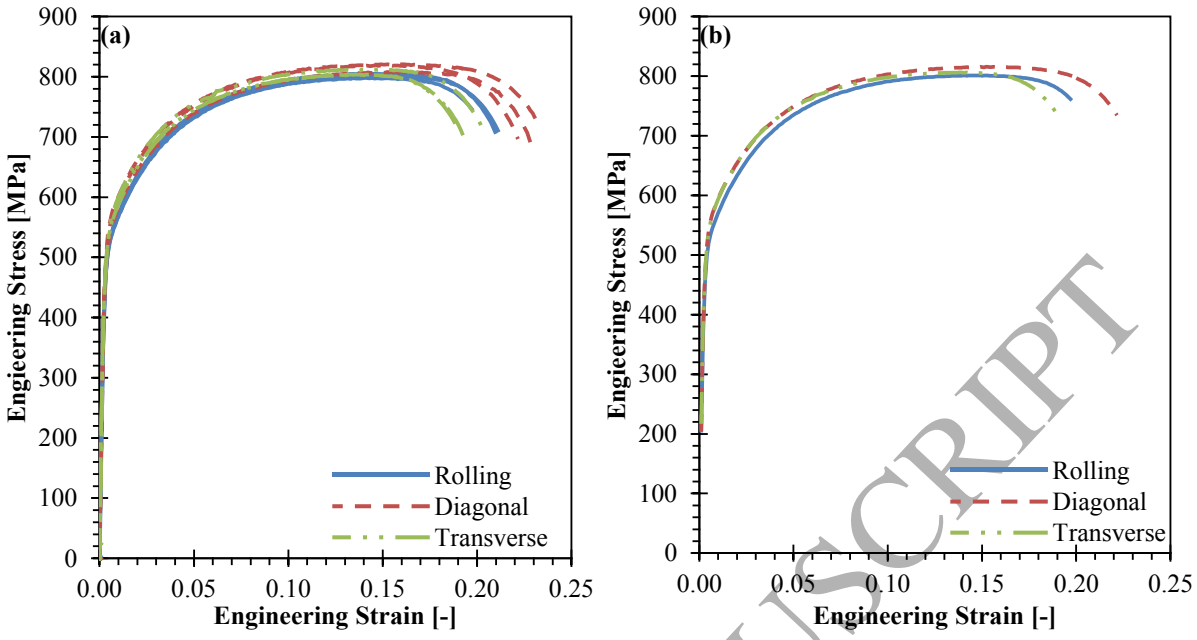

Figure 4 - DP780 uniaxial stress-strain response of rolling, diagonal, and transverse directions at 0.001s^{-1}. (a) repeat tests, (b) average response.

4.1 Identification of the true stress-strain curve to large strain levels

There are several strategies to develop a true stress-true strain curve suitable for input into finite element models based on measured data. Traditional methods use analytical models, e.g. power law hardening, to extrapolate measured stress-strain data beyond the point of uniform elongation. Although simple and effective, these methods can introduce large errors into finite element models if not calibrated correctly. One common source of error that is prevalent with AHSS is the rather low level of strain prior to uniform elongation, rendering the extrapolation prone to large errors at high strains. A recent trend has been to iteratively adjust the input hardening curve such that a finite element model matches the measured stress-strain curve beyond necking [50]. Although it is possible to produce an accurate uniaxial true stress-true strain curve using these inverse methods, post uniform softening due to damage is intrinsically embedded in the input curve. This "linked damage" may be appropriate for simple loading conditions; however, it may be inappropriate or inaccurate for more complex loading conditions (e.g. shear, biaxial, or combined loading) experienced in real structures. Alternatively, hydraulic bulge data can be used to determine the true stress-true strain response to high strains [51, 52]; however, this data was not available for the tested material. In the present work, DIC data was used to directly

measure the true strain, ε_t, in the centre of the neck up to final specimen failure. The true stress, σ_t, was determined based on the true strain, ε_t, and the engineering stress, σ_e, according to:

$$\sigma_t = \sigma_e[1 + (exp^{\varepsilon_t} - 1)]. \quad (14)$$

An error is incurred using this method to determine the true stress-strain response of the material since the specimen is no longer in a state of uniaxial stress once a neck forms as the formation of a neck induces a constraint on the deformation and subsequently a hydrostatic stress to develop. Efforts have been made, by e.g. Bridgman [53], to back out the true uniaxial stress from a necked uniaxial specimen with varying degrees of success. Corrections were not applied to the data in the present work as the material displayed minimal necking up to failure. A modified power law fit based on the work of Ludwik [54] was applied to the measured true stress-true strain curve and extrapolated to facilitate input for finite element calculations. True stress was calculated according to

$$\sigma_t = K\varepsilon_t^n + \sigma_o, \quad (15)$$

where K is the strength coefficient, n is the hardening exponent, and σ_o is a stress offset. Figure 5 shows the true stress-true strain data found using Equation (14) for three representative tests in the transverse direction as solid lines with the power law fit according to Equation (15) extrapolated to a true strain of 1.0 shown as symbols. The transverse direction was adopted as the reference direction as it is the direction with the lowest ductility from the tensile tests. The figure demonstrates a good power law fit to the data as well as the increase in measureable true strain using DIC (0.45) compared to conventional extensometer measurements (0.17).

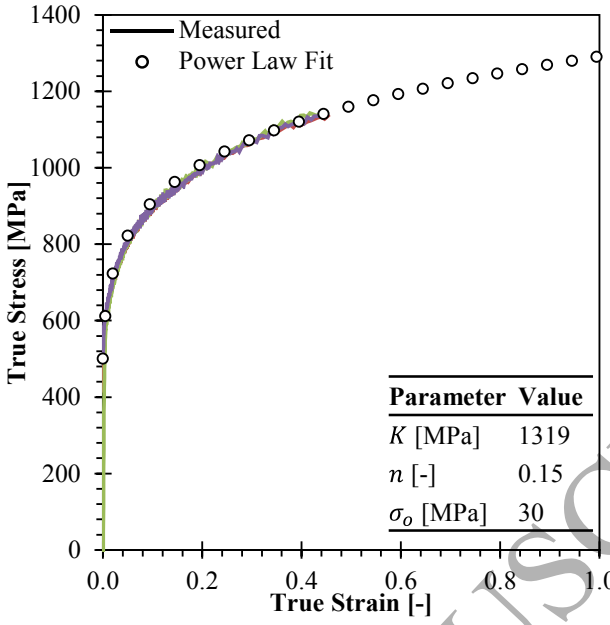

Figure 5 – Measured true stress-true strain data in transverse direction with power law fit.

Figure 6 demonstrates the effectiveness of the preceding method for DP780 as it shows excellent agreement between the measured and finite element predicted engineering stress-strain curves. Note that the finite element model incorporates the same methods and the full GISSMO implementation described later in this work. Additional evidence is provided in the comparison between the DIC measured and finite element predicted strain contours. Both X- and Y-strain contours are shown at an elongation of 0.19 and reveal excellent agreement in the contour shapes and values. The finite element predicted results do show slightly higher peak strains in the neck and can be attributed to a smaller element size compared to that used for the DIC measurements. It is unclear if this relatively simple analysis method is valid for other material systems with more severe anisotropy but for DP780, the method performed very well.

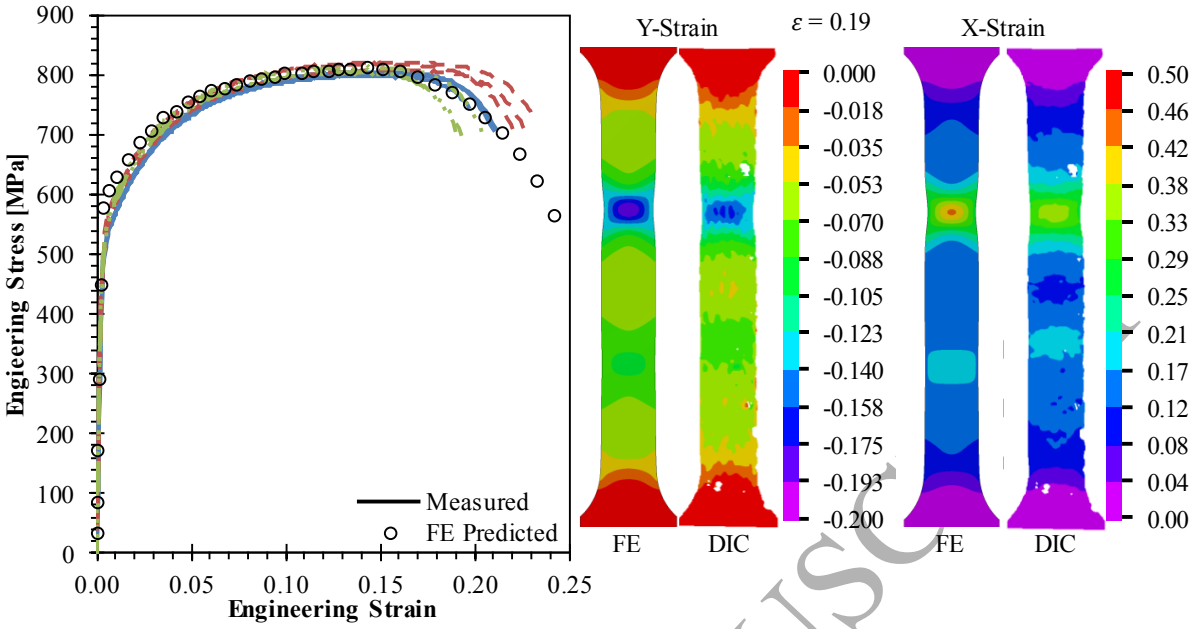

Figure 6 - Comparison of measured and finite element predicted tensile response.

4.2 Butterfly Experiments

Figure 7 (a and b) shows the normalized vertical force as a function of vertical displacement and the normalized horizontal force as a function of vertical displacement of the butterfly specimens as a function of loading angle. The force was normalized by the specimen cross-sectional area to account for variations in specimen machining. Three tests are shown for each condition in the figures. It can be observed in Figure 7a that peak vertical force generally increases and elongation to failure decreases as the loading angle is changed from 0° (shear) to 90° (plane strain tension). Peak vertical force was observed to decrease for loading angles of 5° and 10° and was also observed by Wierzbicki *et al.* [36]. The horizontal forces shown in Figure 7b indicate that some motion occurred in the horizontal direction. As one would expect, there was negligible horizontal force when the specimens were tested in the 90° orientation. Larger horizontal forces were present for the 5°, 10°, 20°, 40°, and 60° orientations due to the asymmetric loading of the specimen. The 0° orientation showed minimal horizontal force up to approximately 1.5mm of vertical displacement followed by a slow increase in force up to specimen failure. Repeatability of the vertical force is good overall for the three repeats while the repeatability of the horizontal force is less consistent for all three repeats.

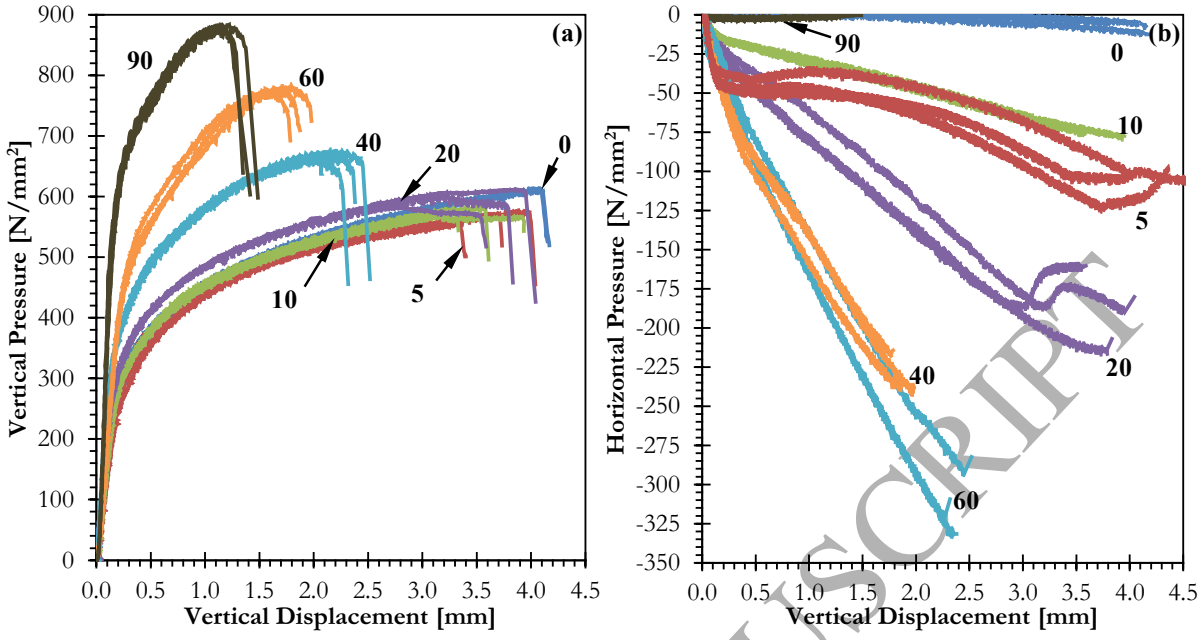

Figure 7 – Normalized load as a function of vertical displacement for butterfly tests. (a) vertical load, (b) horizontal load.

Figure 8 (a and b) shows the Y- and X- displacements of the moving grip, respectively. The displacements for one test in each loading orientation are shown for clarity; however, analysis of multiple tests showed good repeatability of the measurements. In Figure 8a, the measurements obtained using the LVDT mounted to the test fixture are included with the measurements obtained using the fiducial markers and the consistency between the two measurements verifies the Y-displacements. Two X-displacements are shown for each loading orientation in Figure 8b representing each fiducial marker on the moving grip and it can be seen that the displacements do not match during the test (there is an offset between the two displacement curves) except for the 60° and 90° orientations. Close inspection of the initial movements revealed that the X-displacements of each fiducial marker matched during initial specimen loading followed by an offset; thus creating two distinct (but very similar) curves for each loading condition. Subsequent movement was the same after this offset materialized and suggests that a small rotation of the grip occurred as the specimen and fixture were loaded. The root cause of the rotation is not fully understood; however, it was likely a result of some play in the grip system and the asymmetric shape of the system. Had there not been any rotation the X-displacements would have been identical for all loading orientations.

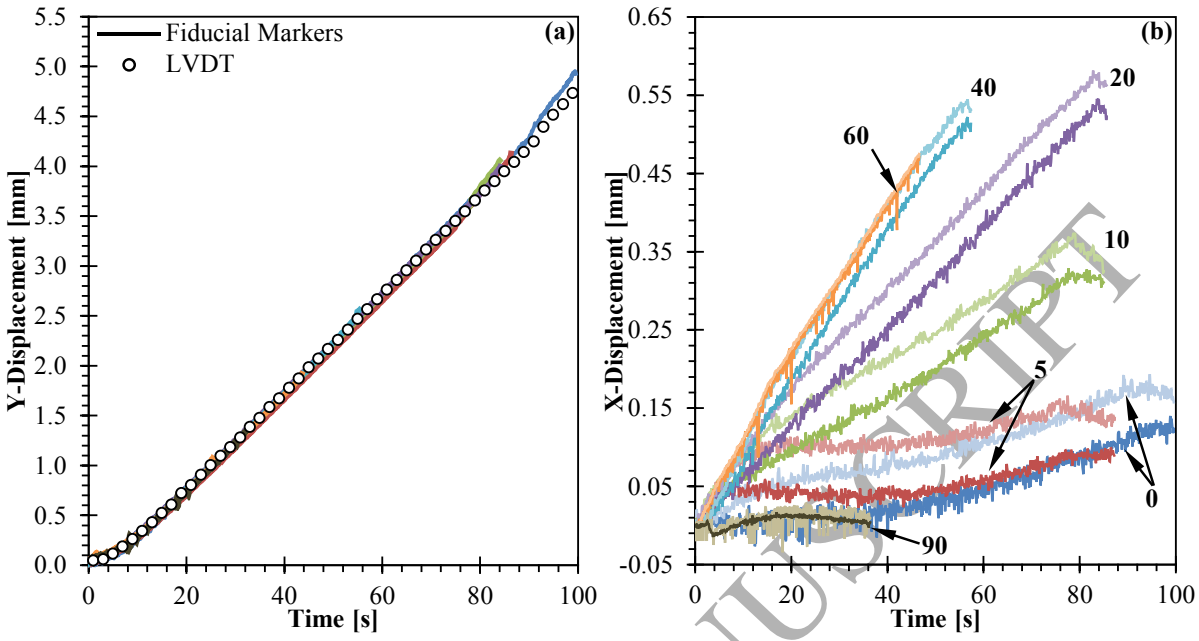

Figure 8 - Moving grip displacements. (a) Y-displacement, (b) X-displacement.

Figure 9 (a and b) shows the Y- and X-displacements of the fixed grip, respectively. The displacements for one test in each loading orientation are shown for clarity; however, analysis of multiple tests showed good repeatability of the measurements. Figure 9a shows similar Y-displacements for the 5°, 10°, 20°, 40°, and 60° loading conditions. The Y-displacements in the 0° and 90° loading conditions may be different from the other orientations as they do not induce a combined loading mode in the specimen. Figure 9b shows the X-displacements and, similar to the moving grip, display evidence of a small rotation of the fixed grip. The total Y- and X-displacements of the fixed grip are small compared to the moving grip, which suggests that they could be safely ignored. However, recent work by Dunand and Mohr [38] discussed the importance of including the boundary condition motion in finite element models to correctly predict specimen strain.

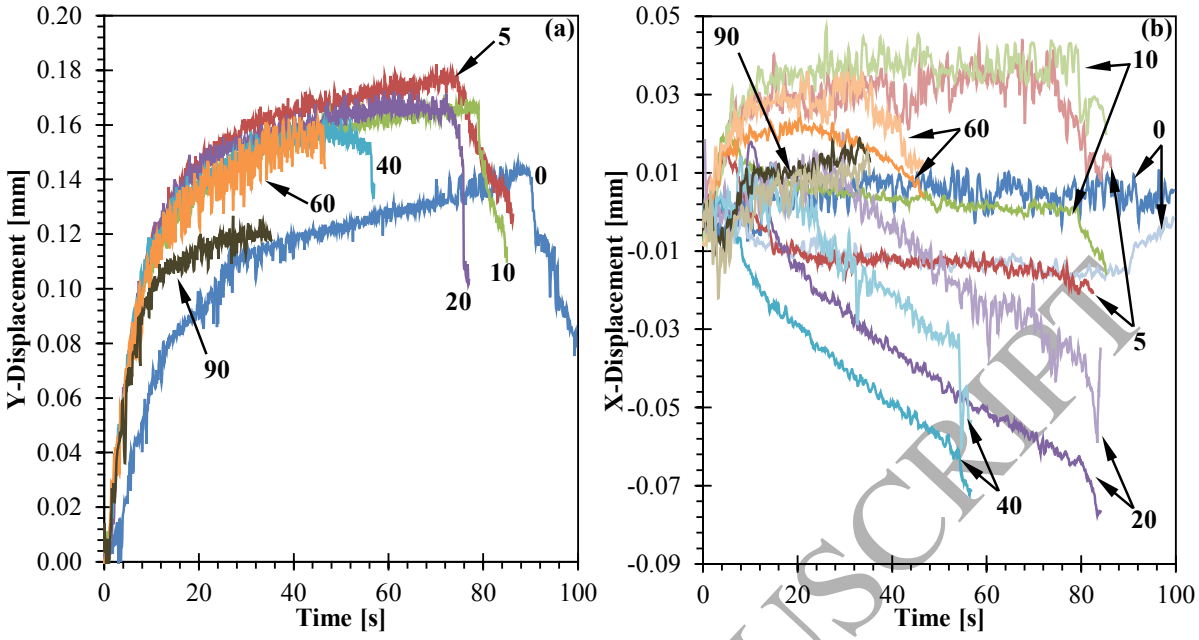

Figure 9 - Fixed grip displacements. (a) Y-displacement, (b) X-displacement.

Rotation of the fixed and moving grip was calculated based on the measured X- and Y-displacements and the results are shown in Figure 10. The calculations showed that the fixed and moving grips rotated in unison; therefore, only one set of data is shown in the figure. The 0° specimen rotates during initial loading of the specimen and then ceases to rotate further. The 90° specimen did not rotate. The 5°, 10°, and 20° specimens rotate identically and rotations decrease as the loading angle decreases as shown by the 40° and 60° specimens. Evidently, grip movement was complex and may be attributed to elasticity in the system. Moreover, careful examination of images acquired during the tests revealed small movements of the specimen at the interface of the grips; therefore, the actual specimen movement near the grip will be used in the finite element models and will be discussed below in Section 5.1.

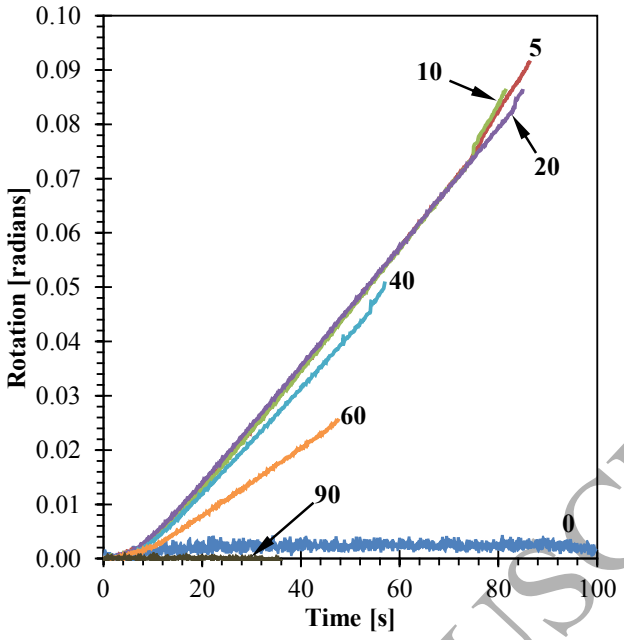

Figure 10 - Calculated rotations.

The butterfly specimen was designed to promote failure at the centre of the reduced section [38]; however, this was not always the case. Plotting the maximum shear strain rate just before failure, as shown in Figure 11 for a loading angle of 0°, demonstrates that the shear band has undergone significant rotation and is interacting with the edge of the reduced section near the shoulder radius. Failure was observed to begin at this shoulder radius for predominantly shear loaded specimens (0°, 5°, 10°, 20°) and likely originated at machining defects despite efforts to minimize stress raisers through careful machining and polishing. Specimens loaded predominantly in tension (40°, 60°, 90°) failed in the centre of the specimen. It was not possible to determine if the specimens failed at the surface or inside the specimen.

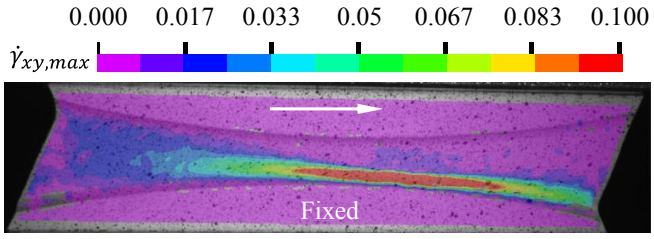

Figure 11 - Maximum shear strain rate for a specimen loaded at 0°.

5.0 Finite Element Models

Finite element models were developed in LS-DYNA [43] to extract failure parameters using the butterfly experimental data. The butterfly model was used to determine the equivalent plastic strain, triaxiality, and normalized Lode parameter at failure of the sheet material. The performance of the models will be compared to experimental load-displacement data and DIC strain data.

5.1 Butterfly Specimen Model

The finite element model of the butterfly specimen consisted of 8-noded, selectively reduced integration, solid brick elements and was solved using implicit time step integration. The element size in the central region of the specimen was chosen to provide 8 elements through the thickness of the reduced section of the geometry with an aspect ratio close to unity in the center of the geometry that created element edge lengths of approximately 0.13mm. Element size was increased away from the reduced section of the model. Symmetry about the XY-plane was exploited and only half of the butterfly specimen was modeled with appropriate boundary conditions applied to the symmetry plane. The motion of the specimen adjacent to the fixture grips was extracted from the DIC data and mapped to the finite element model; therefore, the material clamped within the grips was not accounted for in the model. Material damage and failure were not initially included in the model and isotropic conditions were assumed. Figure 12 shows the finite element mesh of the modeled butterfly specimen in which the inset image is a local magnification of the reduced section of the specimen to illustrate that element quality was high. The butterfly model consisted of 43,776 elements and required between 19 minutes (for the 90° specimen) and 51 minutes (for the 0° specimen) to complete the solution using single precision on a 4-core AMD computer.

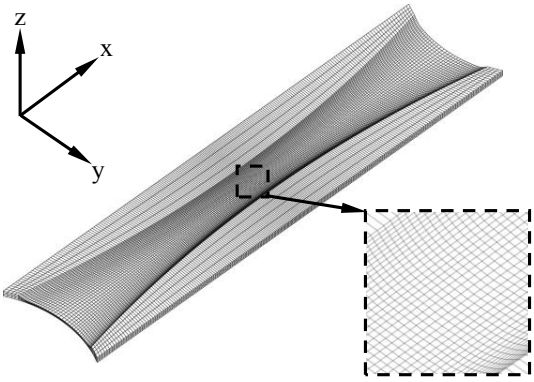

Figure 12 - Butterfly specimen finite element mesh.

Figure 13 (a and b) compares the measured (solid lines) and finite element predicted (symbols) load-displacement in the vertical and horizontal directions, respectively. Only one representative measured curve is displayed for each measured loading condition. As the figure demonstrates, the finite element model accurately reproduces the response in the vertical direction until the specimen eventually fails. (Note that the predictions in Figure 12 include damage and failure treatments using the methods described below.) The finite element model does not predict the horizontal forces with the same accuracy for the shear dominated loading conditions; however, the results are still good especially in light of the very low horizontal force levels.

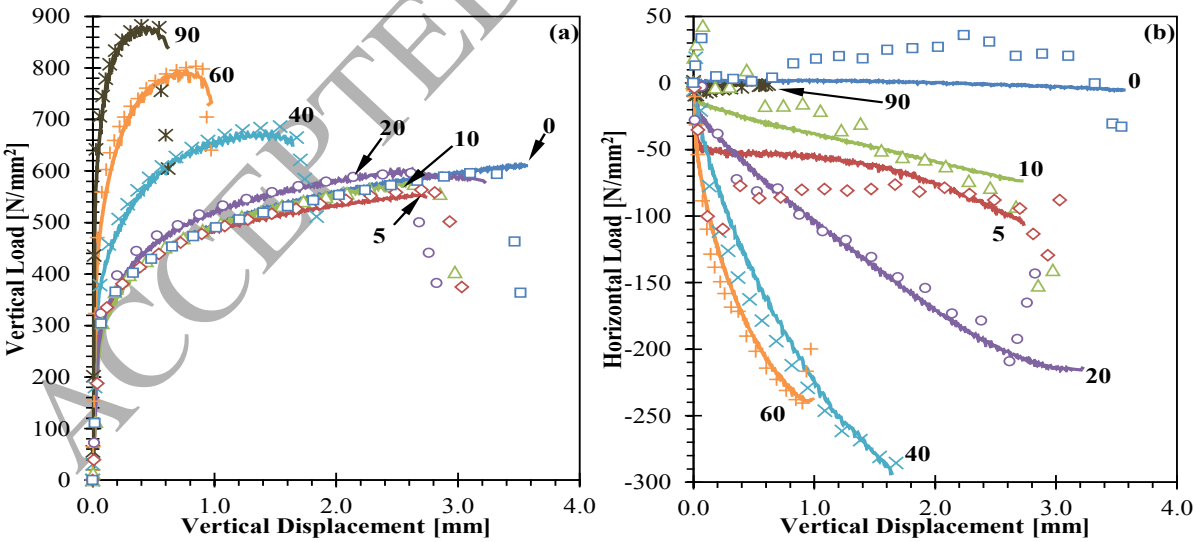

Figure 13 – Comparison of finite element predicted and measured load-displacement data for butterfly specimen. (a) vertical load, (b) horizontal load.

Figure 14 compares the measured and finite element predicted equivalent true strains on the surface of the specimens when maximum load was reached for each loading angle. The figure shows good agreement between the two sets of images in terms of contour shape as well as values. Note that some gaps exist in the DIC data that are caused by calculation difficulties related to sharp corners (where the reduced section begins); this does not affect the strain computation in the gage region. Slight differences between the finite element predicted and measured strain contours could be attributed to anisotropy in the sheet (which may be exacerbated by the machining process) that is not accounted for in the model.

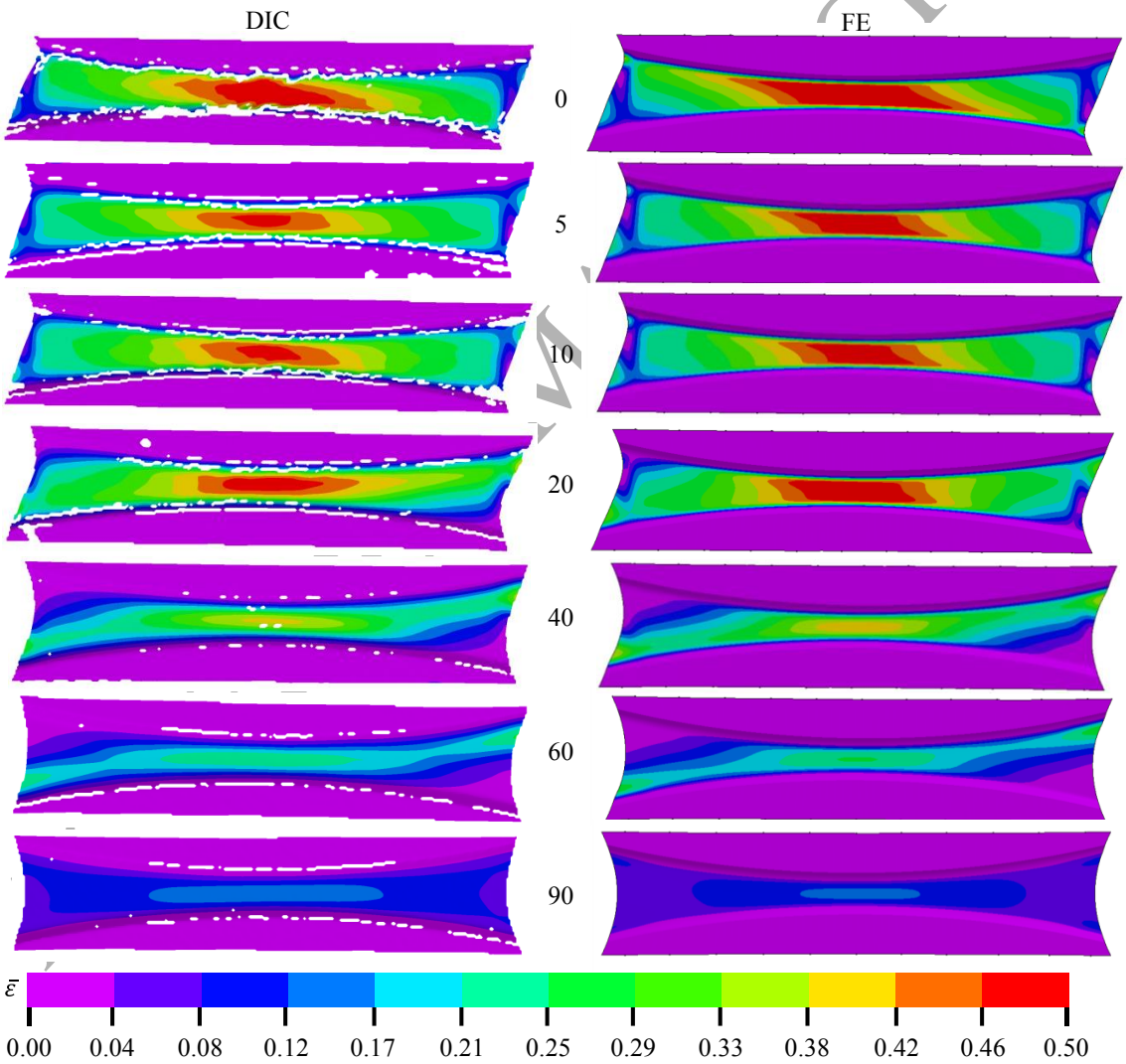

Figure 14 – Comparison between measured and finite element predicted equivalent true strain contours at maximum vertical load.

As the finite element models have been shown to accurately reproduce measured quantities, they can now be used to determine stress state variables for implementation into a fracture surface. It is experimentally challenging to determine if crack initiation occurred on the surface or within the specimen. For the purposes of the present work it was assumed to occur at the central mid-plane for all specimens and, therefore, all finite element quantities were extracted from this location. Comparison of the extracted quantities at the centre and the actual location of failure for the loading conditions that did not produce a central failure did not show appreciable differences. It is acknowledged that this is a potential shortcoming of the presented method and likely results in a lower bound on the results and similar arguments have been made by Dunand [55]. Additional work by Abedini *et al.* [56] compared the shear loading response of the butterfly specimen to a more conventional mini-shear specimen developed by Peirs *et al.* [57] and found that for the same DP780 material used in the present work the butterfly specimen produced similar, but lower, fracture strains compared to the mini-shear specimen. Therefore, the assumptions of central, mid-plane crack initiation resulting in a lower bound estimate appear reasonable. Figure 15 (a and b) shows the predicted equivalent plastic strain as a function of triaxiality and Lode parameter histories for each loading condition, respectively. In Figure 15a, the theoretical triaxialities for shear, uniaxial, and plane strain loading conditions have been added for reference. As the figures demonstrate, some of the loading conditions produce nearly constant stress states (0°, 5°, 90°) while others do not. Ideally, only these constant stress states would be used to calculate a failure surface; however, all of the stress states were used to create a more representative data set. Average triaxiality, η_{avg}, and normalized Lode angle parameter, $\bar{\theta}_{avg}$, values were calculated to account for the stress histories according to:

$$\eta_{avg} = \frac{1}{\bar{\varepsilon}_f} \int_0^{\bar{\varepsilon}_f} \eta d\bar{\varepsilon}_p \tag{16}$$

and

$$\bar{\theta}_{avg} = \frac{1}{\bar{\varepsilon}_f}\int_0^{\bar{\varepsilon}_f} \bar{\theta}\, d\bar{\varepsilon}_p \tag{17}$$

The dashed line in Figure 15 (a and b) is a fit to the failure data using the procedures described by Lou and Huh [26] and shows a good prediction of the data. Interested readers should refer to Lou and Huh's work for model calibration details. The parameters used in the fit are included in Figure 15b. This fitted data will be used in the verification and validation cases to produce a smooth failure surface input curve.

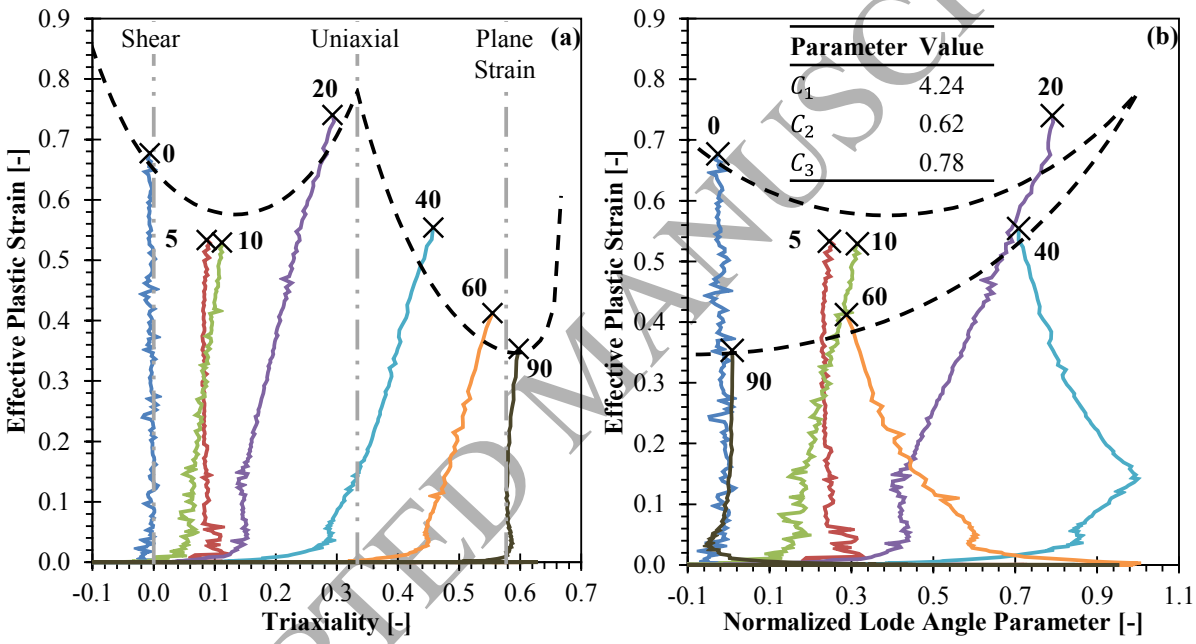

Figure 15 - Failure locus from butterfly tests. (a) triaxiality space, (b) normalized Lode angle parameter space.

5.2 Verification

Verification of the failure parameters extracted from the finite element models was performed by re-simulating the butterfly models with GISSMO active and comparing the measured and predicted displacement at failure and location of crack initiation. The results of the butterfly model with GISSMO are shown in Figure 13. The model predicted peak load, vertical displacement at failure, and the strain contours show good agreement to the experimental data. Figure 16 compares the excellent correlation between the model predicted crack initiation sites to

the experimental observations for each loading angle. The DIC experimental observations show contours of maximum shear strain rate, with the observed initiation site indicated by the intense contour localization. The good predictions of the simulations of the butterfly experiments are to be expected in that the stress states have been extracted, averaged, and then used to calibrate the damage model based on the failure strains corresponding to the experimental displacements. This closed-loop validation is important to understand how well the model can recreate the experiments and provide confidence in the failure locus for the relatively proportional loading conditions used in its development. It is important to emphasize that severely non-proportional stress (or strain) paths have not been considered in the fracture locus calibration and the model can only be strictly valid for the proportional stress states used in its calibration. To properly evaluate the performance of the failure surface, a series of independent validation experiments and simulations will be performed in the subsequent sections.

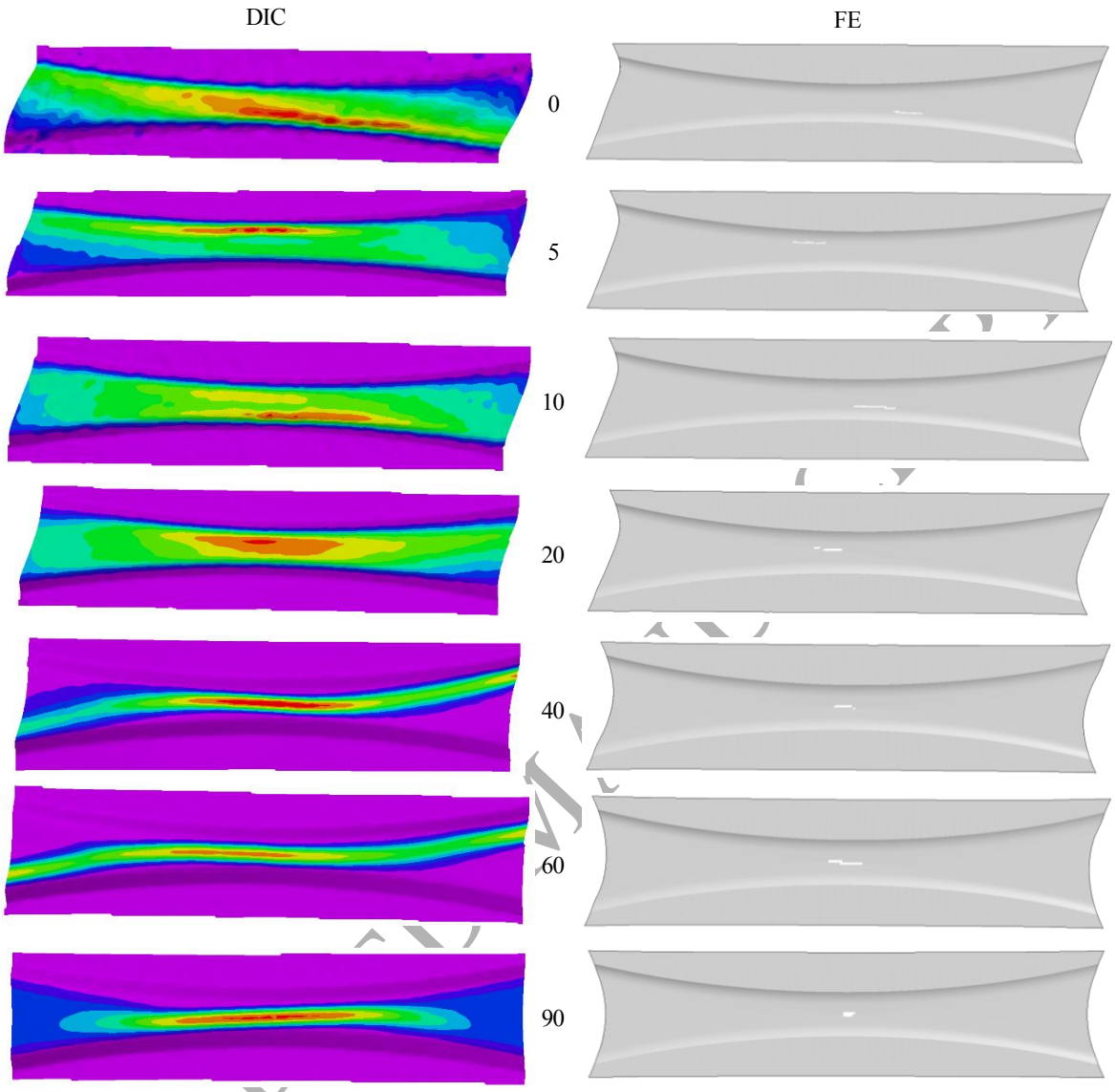

Figure 16 - Comparison between experimentally observed and finite element predicted crack initiation locations.

6.0 Validation

Four independent validation tests were performed to assess the performance of the extracted failure parameters and included a hole tension test, flat and conical hole expansion tests, and a hemispherical punch test. These tests were chosen as they are significantly different from the tests used to obtain the failure parameters and represent a broad range of stress states; therefore, accurate prediction of these tests indicates a robust set of failure parameters. The chosen

validation tests incorporate generally monotonic loading paths; therefore, the non-proportional damage treatment of GISSMO is not being evaluated and is the subject of future work. The same material lot used to determine the constitutive and failure parameters was used for the validation tests. The experimental methods and results for each validation test will be discussed and compared to finite element models developed using the constitutive and failure parameters determined above.

6.1 Hole Tension Test

The hole tension test is similar to a uniaxial tension test; however, a central hole is machined into the middle of the gauge section which alters the state of stress. A 10 mm diameter hole was fabricated by drilling and reaming followed by manual polishing with 1200 grit SiC paper to remove any traces of a burr or edge imperfection to mitigate premature cracking. The geometry used in the present work was based on the findings of Bao [58] and is shown in Figure 17 with relevant dimensions. The hole tension tests were performed using the same equipment and procedures as the uniaxial tension tests as discussed in Section 3.0. Specimen alignment was carefully controlled to ensure even loading on either side of the machined hole.

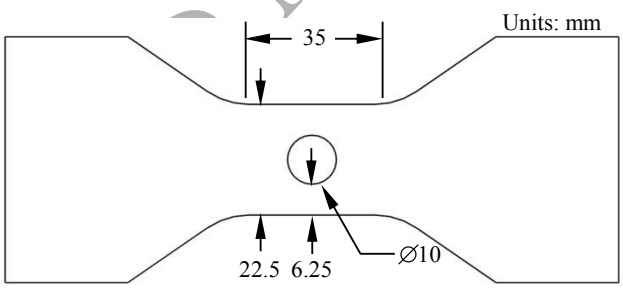

Figure 17 - Hole tension specimen geometry.

Figure 18 shows the finite element mesh of the modeled hole tension geometry in which the inset image is a local magnification of the reduced section of the specimen to illustrate mesh topology near the hole. Symmetry about the XY- and XZ-plane was used with appropriate boundary conditions applied. Material outside of the reduced section of the specimen was not modelled to reduce computational effort; examination of the DIC strain fields showed acceptably low deformation in these regions. A velocity profile was applied to the end of the specimen to match

that used during the experiments. Nodes were placed in the finite element model corresponding to the location of the extensometer used in the DIC software so as to accurately match the displacement history of the experimental tests. The element size around the hole was 0.13mm with an aspect ratio of approximately unity to match that used in the butterfly model resulting in a model consisting of 12,240 elements and requiring 39 minutes to complete the solution using single precision on a 4-core AMD computer.

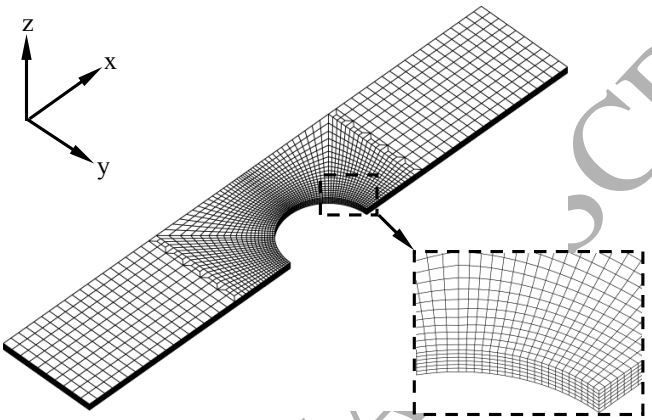

Figure 18 – Hole tension specimen finite element mesh.

Figure 19 compares the measured (solid line) and finite element predicted (symbols) nominal stress-strain response of the hole tension test and shows that the model is able to accurately predict the measured response. Only one representative measurement is shown for clarity; however, multiple tests showed good repeatability. Figure 20 (a, b and c) provides additional qualitative evidence of the accuracy of the finite element predictions. Figure 20a shows the mid-thickness face of the finite element model and demonstrates that failure was predicted inside the specimen and away from the edge of the hole, which is supported by Figure 20 (b and c) and was also reported by Lou and Huh [59]. Figure 20b shows an etched micrograph of a partially failed hole tension specimen that shows intense strain localization in the form of elliptical-shaped banding, where the centre of the ellipse appears to be located near the crack tip. Figure 20c shows a large void present at mid-thickness of a representative DP600 hole tension specimen before crack initiation occurred where the size and location of the void are also in good agreement with the DP780 finite element predictions. Efforts were made to capture the onset of fracture in the current DP780 material in a manner similar to that in Figure 20c; however, it was

difficult to stop the test after such a large void had nucleated and before a crack had propagated. Note that the authors are not implying that the location of failure would be the same for two different alloys; rather, the location of the void in the DP600 specimen is being used to illustrate and support the argument that crack initialization can occur away from the hole's edge. Indeed, as shown by Roth and Mohr [60], the location of failure in a hole tension test is highly dependent on the material properties and specimen geometry. Based on the micrographs and the finite element model it is hypothesized that intense strain localization occurred away from the edge of the hole leading to void nucleation and growth. This in-turn increased the strain in the ligament at the edge of the hole. Once this ligament failed a crack started to propagate from the edge of the hole and through the specimen. It is also plausible that the finite element predictions are for ideal conditions with perfect edge quality leading to failure away from the hole. Damage due to machining may lead to failure starting at the edge of the hole. It is expected that an anisotropic material model would better capture localization just behind the hole edge.

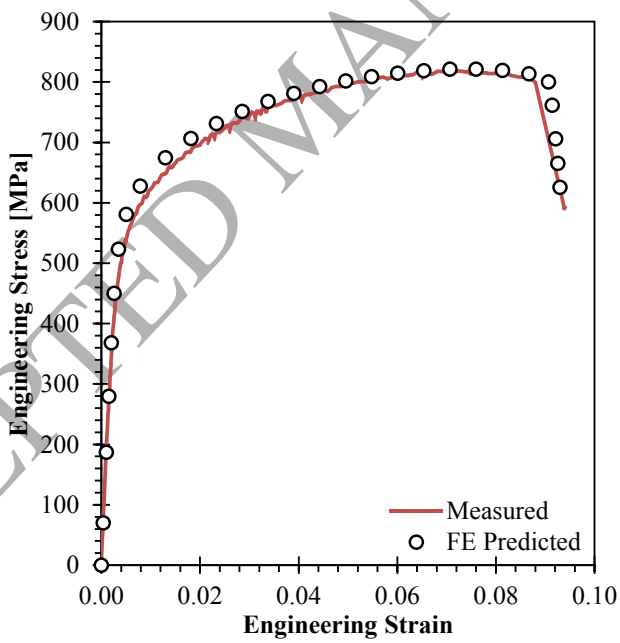

Figure 19 - Comparison between measured and finite element predicted engineering stress-strain for the hole tension test.

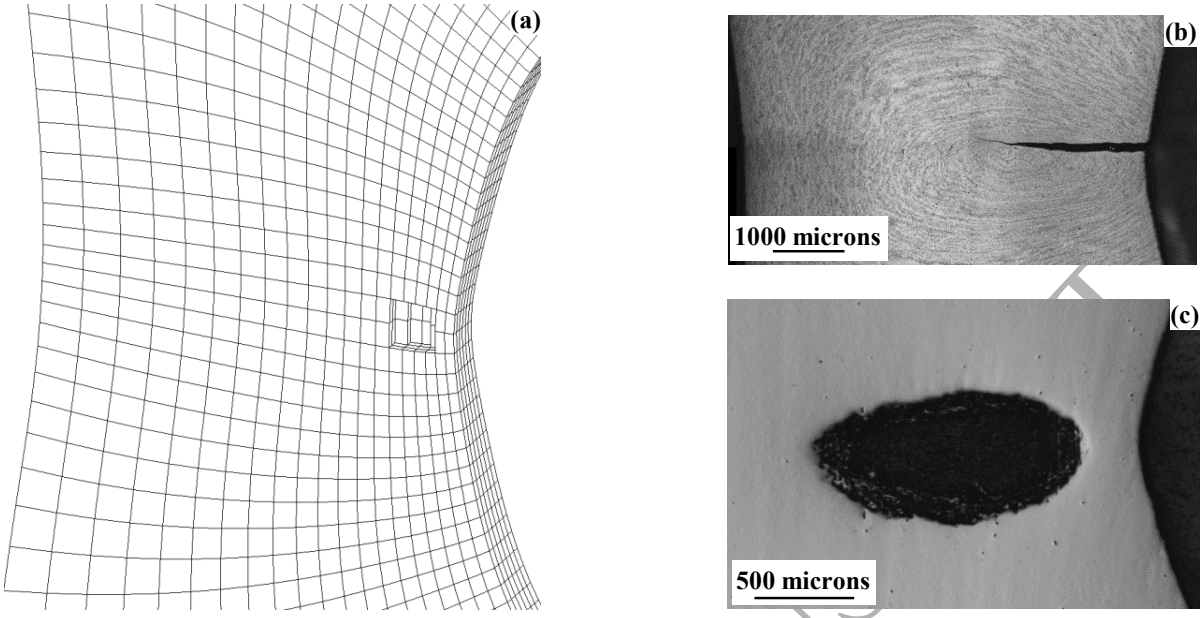

Figure 20 - Comparison between measured and predicted failure initiation location. (a) finite element predicted, (b) etched DP780 micrograph, (c) polished DP600 micrograph.

6.2 Hole Expansion Tests

Hole expansion tests are common industrial operations used to determine the edge formability of sheet metal. The test is performed according to ISO standard 16630:2009 [61] by forcing a conical or flat tool through a hole, in the present work, machined into a blank. A greater expansion of the hole diameter prior to failure indicates a material less prone to edge cracking. It is important to state that a reamed (machined) hole and not a sheared hole was used in the experiments to avoid modelling the complex shearing process and strain distribution at the edge. A machined hole is used to match the finite-element model of the test where the hole edge quality is "ideal". Previous work [62, 63, 64] reported lower edge formability while using a flat punch compared to a conical punch. Figure 21 shows a cross-section of the hole expansion processes adopted in the present work and performed at ArcelorMittal Dofasco. The blank measured 130 x 130 mm with a reamed 10 mm pilot hole in the center, a sufficiently high blank holder force was applied to prevent draw-in (minimum of 50kN), the holding diameter was 52 mm, and the draw ring had a 60 mm diameter opening with a 12mm corner radius. The blank, binder, and draw ring were identical for all tests. The conical punch had a diameter of 50 mm with a 60° included angle. The flat punch had a diameter of 50 mm with a 9 mm corner radius

and incorporated a 25 mm diameter relief to prevent the edge of the blank from rubbing on the punch. Punch speed was a constant 1mm/s for both tools. A light oil film was applied to the blank to lubricate the punch-blank interface. An imaging system was in place above the apparatus to record the diameter of the expanding hole. The bottom edge of the hole was used to determine the hole expansion ratio (HER), which is found from:

$$HER = \frac{d_f - d_i}{d_i}, \tag{18}$$

where d_f and d_i are the final and initial diameters of the hole. The test is halted and the final diameter is measured under load when the first through thickness crack appears. A detailed description of the hole measurement technique is provided by Pathak *et al.* [64]. A minimum of 10 tests was performed to obtain a statistically significant sample size. Load was not measured during testing at Dofasco; additional testing was performed at the University of Waterloo with the same tooling to measure load-displacement and surface strains with DIC. The hole expansion ratio was found to be the same at both locations.

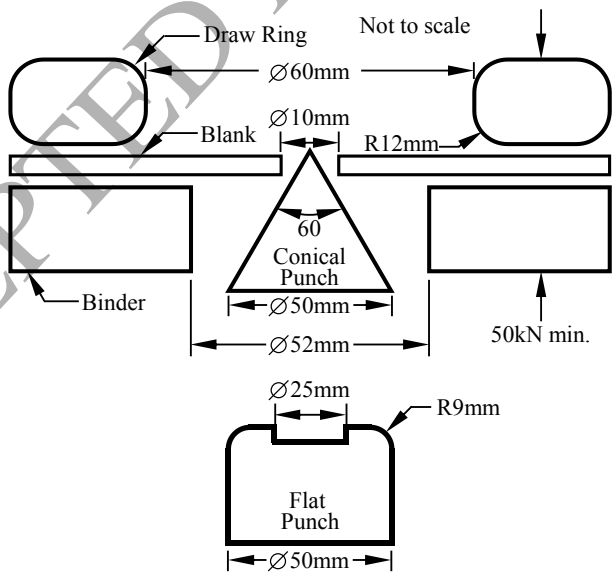

Figure 21 - Hole expansion test experimental setup.

Symmetry about the XZ- and YZ-planes was exploited and as such only one-quarter of the geometry was meshed to reduce the number of elements and solution time. Appropriate boundary conditions were applied to the symmetry faces. All tooling was assumed rigid and was discretized using rigid shell elements. Figure 22 shows a representation of the finite element mesh for the conical tool with the inset image demonstrating the mesh detail at the edge of the hole; the mesh for the flat punch model was similar but is not included for brevity. A penalty function-based contact definition was used between the tooling and the blank. A coefficient of friction of 1.0 was used between the binder/draw ring and the blank to simulate a knurled surface. The coefficient of friction between the punch and the blank was not measured; however, a value of 0.2 was found to result in a load-displacement response that matched the measured behaviour. This value was thought reasonable for this situation involving a light machine oil lubricant between the punch and blank. The element size around the hole was 0.13mm with approximately unity aspect ratio to match that used in the butterfly model; element size was increased away from the hole resulting in a model consisting of 51,000 solid elements for the blank and 14,400 shell elements for the rigid tooling. 73 and 84 minutes were respectively required to solve the conical and flat models on a desktop computer with a 4-core AMD CPU.

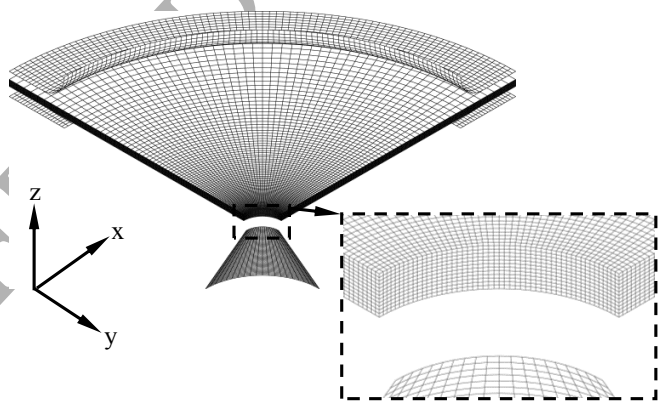

Figure 22 – Conical hole expansion finite element mesh.

Figure 23a shows a typical load-displacement curve for the conical punch test. The solid lines are representative experimental data while the symbols are the finite element model predictions. The figure shows that the model accurately predicted the observed load-displacement response with a peak load of 24.8kN, which is close to the observed value of 24.8kN. Table 1 lists the

experimentally observed average and standard deviation HER and peak load, and finite element predicted HER and peak load for the conical punch and shows that the predicted HER was well within the scatter of the observed HER. A crack was assumed to have occurred in the model when the first element had been deleted and the corresponding hole diameter was used to calculate the predicted HER.

Table 1 – Measured and finite element predicted hole expansion ratios and peak loads for conical and flat punch geometries.

Punch Geometry	Measured HER [%]	Predicted HER [%]	Measured Peak Load [kN]	Predicted Peak Load [kN]
Conical	51.0±10.0	53.0	24.8±0.1	24.8
Flat	39.0±2.8	36.4	77.5±0.9	79.6

Figure 23b shows side-by-side images of the observed and predicted holes at the time of crack initiation for the conical punch. The images have been scaled to the same linear dimensions. The predicted HER agrees well with the measured value, although some differences can be observed in the figure with respect to the predicted and observed crack location (around the hole) and orientation through the blank thickness. These differences are attributed to the isotropy assumption in the model. Experimentally, cracking always initiates in the rolling direction which corresponds to tensile loading in the transverse direction due to the circumferential loading of the hole. The transverse direction also has a higher stress ratio relative to the rolling direction and the lowest ductility so it is not unexpected that the isotropic model does not capture localization and failure initiating at the rolling direction as in the experiment. Figure 23c compares the measured and finite element predicted equivalent true strain contours at a HER of 37% and shows good agreement. DIC strains could not be computed on the inner hole surface as it is not initially visible during the test; it only becomes visible as the sheet is expanded by the tooling and explains the apparent discrepancy at the edge of the hole where the highest strain levels are achieved. Detailed analysis of the strain history near the hole should therefore be conducted using a finite element model as opposed to DIC. Agreement of the load-displacement curve, HER, and strain contours indicates a well formulated model.

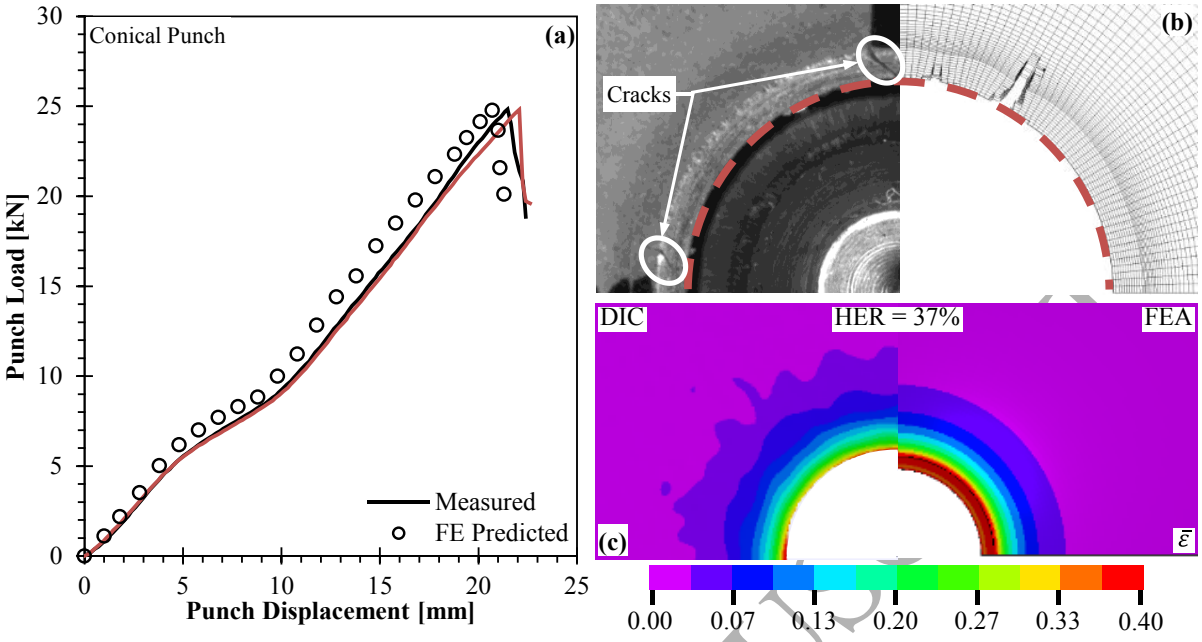

Figure 23 - Comparison between measured and finite element predicted quantities for the conical hole expansion test. (a) load-displacement, (b) crack pattern, (c) equivalent true strain contours. Note that measured DIC contours cannot be capture for the inside edge of the hole.

Figure 24a shows a typical load-displacement curve for the flat punch test. The solid lines are representative experimental data while the symbols are the finite element model predictions. The figure shows that the model accurately predicted the observed load-displacement curve with a predicted a peak load of 79.6kN, which is close to the observed value of 77.5kN. Table 1 lists the experimentally observed average and standard deviation HER and peak load, and finite element predicted HER and peak load for the flat punch and shows that the predicted HER was well within the scatter of the observed HER. A crack was assumed to have occurred in the model once a line of elements had been deleted through the blank thickness and the corresponding hole diameter was used to calculate the predicted HER. Figure 24b shows the predicted crack initiation for the flat punch and the measured DIC equivalent true strain contours. The images have been scaled to the same linear dimensions. Some differences can be observed in the figure with respect to the predicted crack location and the maximum strain. The DIC measurements demonstrate some in-plane anisotropy in the strain contours, where the strains localize in the transverse direction and failure initiates behind the hole edge. The finite element model predicts failure away from the hole edge and, since isotropic conditions were assumed, not aligned with either the rolling or transverse directions. Failure away from the hole

edge is logical when considering an initially damage-free material since triaxiality transitions from nearly uniaxial at the hole edge to nearly biaxial at the radius of the punch.

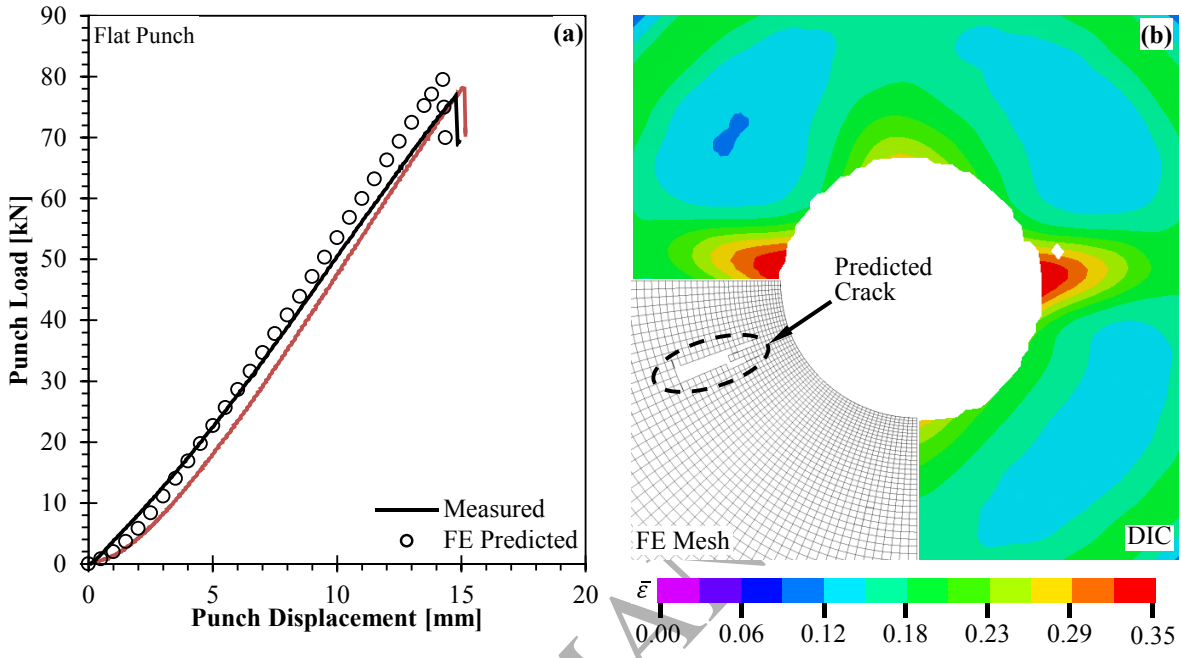

Figure 24 - Comparison between measured and finite element predicted quantities for the flat hole expansion test. (a) load-displacement, (b) effective strain contours and crack pattern.

6.3 Hemispherical Punch Test

Hemispherical punch tests (also known as Limit Dome Height tests) are common operations used to determine the biaxial formability of sheet metals. The test is performed by forcing a solid hemispherical punch into a clamped specimen until failure occurs in the specimen. Figure 25 shows a cross-section of the hemispherical punch test adopted in the present work. The blank measured 200 x 200mm, the blank holder force was 650kN, the binder diameter was 105mm, the lock bead diameter was 135mm, and the draw ring had a 105mm diameter opening with a 6mm corner radius. The punch had a diameter of 100mm. Punch speed was a constant 1mm/s. Alternating layers of petroleum lubricant and Teflon sheets were placed between the punch and specimen to minimize friction.

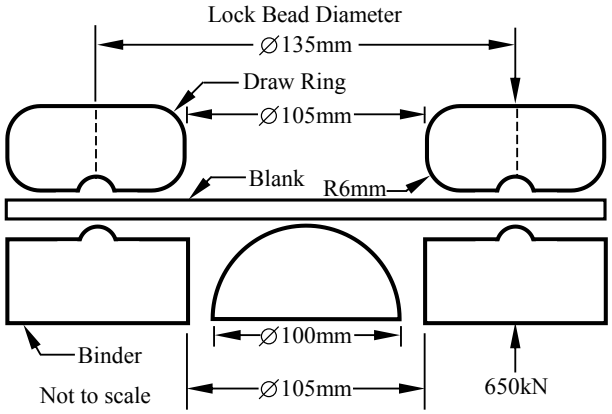

Figure 25 – Hemispherical punch test experimental setup.

Symmetry about the XZ- and YZ-planes was exploited and as such only one-quarter of the geometry was meshed to reduce the number of elements and solution time. Appropriate boundary conditions were applied to the symmetry faces. All tooling was assumed rigid and was discretized using shell elements. Figure 26 shows a representation of the finite element mesh for the hemispherical punch test with the inset image demonstrating the mesh quality at the center of the blank. A penalty function-based contact definition was used between the tooling and the blank. A coefficient of friction of 1.0 was used between the binder/draw ring and the blank to simulate a knurled surface. The coefficient of friction between the punch and the blank was not measured; however, a value of 0.1 was found to produce a load-displacement response that matched the measured behaviour. This value was thought reasonable for this situation involving a Teflon and lubricant stack separating the tooling from the specimen. Element size at the center of the blank was 0.13mm with approximately unity aspect ratio to match that used in the butterfly model; element size was increased away from the symmetry point resulting in a model consisting 42,192 solid elements for the blank and 9,000 shell elements for the rigid tooling. 97 minutes were required to solve the model using single precision on a desktop computer with a 4-core AMD CPU.

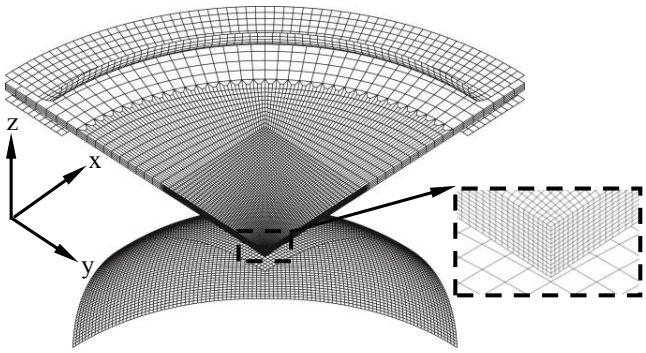

Figure 26 – Hemispherical punch finite element mesh.

Figure 27a shows a typical load-displacement curve for the hemispherical punch test. The solid lines are representative experimental data while the symbols represent the finite element model predictions. The figure shows a good model prediction compared to the observed load-displacement data. The predicted peak load of 202.8kN is high compared to the observed value of 167.9kN; however, the predicted displacement to failure is in good agreement with observations. Over prediction of the load may be associated with the extrapolated hardening curve generating too great a stress for the relatively high strains that can be achieved in the biaxial condition. Figure 27b shows the finite element predicted and the measured DIC equivalent true strain contours just before failure initiates. The images have been scaled to the same linear dimensions. Overall, there is a good visual match between the strain contours. A crack was observed to propagate along the transverse direction; however, the finite element model predicted cracks forming simultaneously in the rolling and transverse directions due to isotropic material assumptions. It is important to mention that although the failure locus was not calibrated directly with a biaxial test, there may be some good fortune associated with the good correlation between FE predictions and observations. The biaxial tests were performed after the butterfly tests were completed and the close agreement with the biaxial test was unexpected. It is also possible that the good correlation was due to the accurate prediction of the shape of the failure locus in this region using the Lou and Huh failure locus model (Equation (10)) but this result should only be considered for the present DP780 alloy.

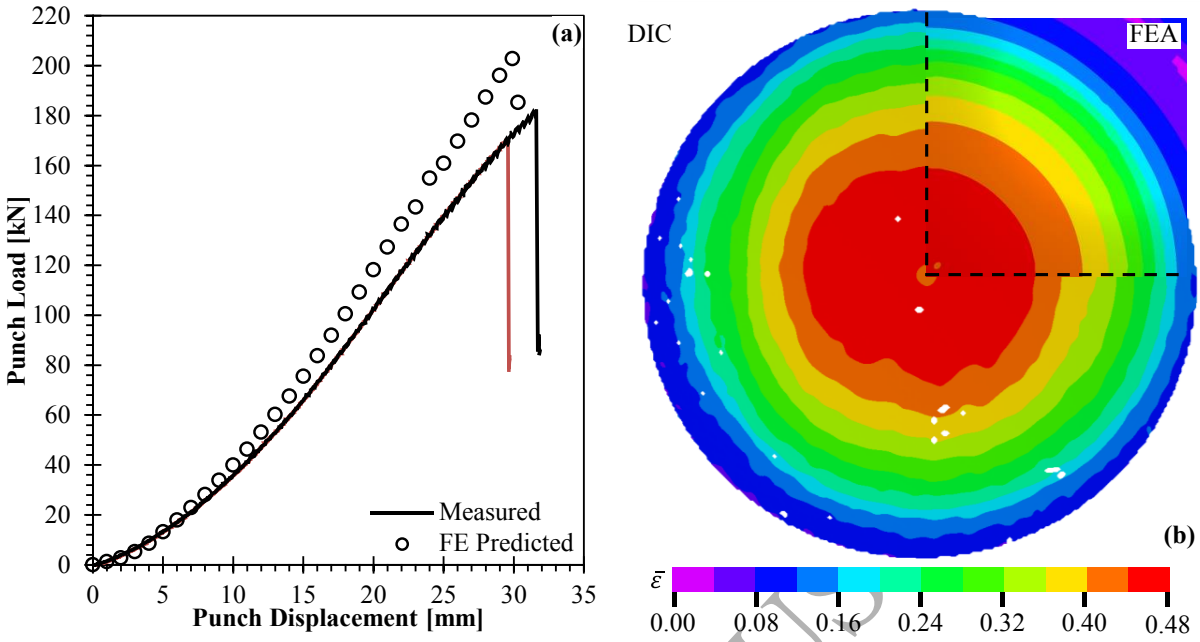

Figure 27 - Comparison between measured and finite element predicted quantities for the hemispherical punch test. (a) load-displacement, (b) equivalent true strain contours.

7.0 Discussion

The butterfly specimens have been shown to produce a broad range of stress states suitable for fitting to a published failure surface. The validation and verification results demonstrate the accuracy and usability of the developed failure parameters. Of particular importance is the ability to predict failures in the biaxial stress state with the hemispherical punch test as this stress state was not included in the experimental data obtained from the butterfly tests. However, it should be stressed that the parameters identified in the present work are a function of the model assumptions, such as constitutive model, element type, solution procedure, and damage formulation, and post-uniform softening treatment. Nevertheless, the results demonstrate the applicability of the chosen test specimens, failure model, and damage accumulation model to simulating industrial tests; however, some questions remain.

One of the disadvantages of the butterfly specimen is the necessity to machine through the sheet thickness to encourage centre failure. This machining may introduce damage to the sheet that would reduce deformation prior to failure. Moreover, machining marks may provide failure initiation sites that may not be present in the as-received sheet. Despite careful machining and

specimen polishing to minimize these effects, residual damage likely remains, as such the developed failure locus should be considered a lower bound.

All testing was performed at quasi-static rates, whereas many forming operations are performed at moderate strain rates to enhance productivity. The GISSMO model implemented in LS-DYNA does provide scaling of failure as a function of strain rate. As shown by Anderson *et al.* [6] this sheet material has minimal sensitivity to increases in strain rate in the uniaxial condition up to approximately $1s^{-1}$, above which peak stress and true failure strain increased; however, sensitivity to increases in strain rate increased as triaxiality increased when using notched tensile specimens. It may be suitable to scale the failure parameters of the present work according to the results of Anderson *et al*. [6] provided triaxiality-dependent scaling is performed. It could be argued that most forming operations experience strain rates on the order of $1s^{-1}$ or less, which may negate the need to scale the failure parameters as a function of strain rate. Deformations during crash are typically in the range of 100 – $1000s^{-1}$; therefore, scaling should be performed. Performing the butterfly tests of the present work at elevated loading rates would lead to a more thorough understanding of the effects of strain rate on the shape and magnitude of the failure surface.

From a practical perspective, it is important to emphasize that all simulations were performed with solid elements with similar element sizes in critical regions of approximately 0.13 mm. This is not a typical mesh size or element type for industrial applications. For example, sheet metal forming and vehicle crash simulations employ considerably larger shell elements. Larger element size can be accounted for using mesh regularization routines where scaling is used to adjust equivalent plastic strain to failure as element size is increased. Shell elements do not require a failure surface; therefore, Lode dependence is not required. Analysis of the triaxiality and Lode values obtained from the present work showed that nearly plane stress conditions were obtained for the 0, 5, 10, and 20° loading conditions according to [30]

$$-\frac{27}{2}\eta\left(\eta^2-\frac{1}{3}\right)=\sin\left(\frac{\pi}{2}\bar{\theta}\right); \tag{19}$$

however, some tests did not maintain plane stress conditions (40, 60, 90°) and may be transitioning towards plane strain (as the 90° loading condition should). The data that does not conform to plane stress conditions could be excluded from the fitting procedure of a simplified 2D failure locus in equivalent plastic strain and triaxiality space; however, a poor fit could be obtained depending on which data points are neglected. Alternatively, the procedure described in the present work could be followed and the appropriate 2D failure locus extracted from the 3D failure surface. It is the opinion of the present authors that developing a 3D failure surface is more appropriate as it provides additional data that could be used for in-depth analysis of components that may warrant extra data.

A final consideration that should be addressed is the isotropic assumption. Most of the presented tests did not show strong anisotropy in the bulk response of the material. Anisotropy was apparent during the hole expansion and hemispherical punch tests where failure predominantly occurred in the tangential direction. This preferred failure direction may be associated with microstructural features brought on by sheet chemistry and processing conditions and could also explain the reduced uniaxial elongation to failure in the tangential direction. It is expected that an anisotropic plasticity model along with the proposed isotropic failure model would significantly improve prediction of the failure location in the hole expansion tests as plastic strain localization would occur in the preferred failure direction, spurring damage development and failure at that location. Additionally, an anisotropic failure surface could be measured and used in conjunction with an appropriate anisotropic yield surface should desired model fidelity warrant an accurate prediction of failure direction. Considering the quantity of testing required and the potential scatter in the failure data it may be more effective to use an isotropic failure locus and an anisotropic yield surface. The above methodology was published by Lou *et al.* [65] with good results during the completion of the present work.

8.0 Conclusions

The presented work has developed a failure surface for dual-phase 780 steel sheet using a butterfly specimen optimized by Dunand and Mohr [38]. A custom fixture, inspired by the work of Wierzbicki *et al.* [36], was used to index the specimens generating a range of equivalent

plastic strains to failure, triaxialities, and Lode parameters covering stress states from shear to plane strain tension. Digital image correlation was used to measure the surface strains. A numerical model of the butterfly specimens was used to extract the failure surface parameters and a smooth surface was fit to the data. The GISSMO damage model available in LS-DYNA was used to predict failure of the butterfly specimens as well as four independent validation tests.

The results showed that the developed failure surface and finite element model could predict the load-displacement and the surface strains of the butterfly specimens. Independent validation tests showed the versatility of the model by predicting the load-displacement and surface strains of these tests as well. The failure direction of the validation tests was not predicted due to the isotropic assumption of the model.

Acknowledgements

Financial support from Cosma International, Automotive Partnership Canada (APC), the Natural Sciences and Engineering Research Council of Canada (NSERC), Ontario Research Fund, and the Canada Research Chairs Secretariat are gratefully acknowledged. The authors thank ArcelorMittal Dofasco for providing access to the hole expansion apparatus and a special thanks to Sante DiCecco for his assistance with the DIC analysis of the butterfly specimens.

References

[1] W. Joost, "Reducing Vehicle Weight and Improving U.S. Energy Efficiency using Integrated Computational Materials Engineering," *JOM,* vol. 64, pp. 1032-1038, 2012.

[2] U.S. Department of Energy, "Materials Technologies: Goals, Strategies, and Top Accomplishments," 2010.

[3] J. Huh, H. Huh and C. Lee, "Effect of Strain Rate on Plastic Anisotropy of Advanced High Strength Steel Sheets," *International Journal of Plasticity,* vol. 44, pp. 23-46, 2013.

[4] J. Kim, D. Kin, H. Han, F. Barlat and M.-G. Lee, "Strain Rate Dependent Tensile Behavior of Advanced High Strength Steels: Experiment and Constitutive Modeling," *Materials Science and Engineering A,* vol. 559, pp. 222-231, 2013.

[5] S. Winkler, A. Thompson, C. Salisbury, M. Worswick, I. van Riemsdijk and R. Mayer,

"Strain Rate and Temperature Effects on the Formability and Damage of Advanced High-Strength Steels," *Metallurgical and Materials Transactions A,* vol. 39A, pp. 1350-1358, 2008.

[6] D. Anderson, S. Winkler, A. Bardelcik and M. J. Worswick, "Influence of Stress Triaxiality and Strain Rate on the Failure Behavior of a Dual-Phase DP780 Steel," *Materials and Design,* vol. 60, pp. 198 - 207, 2014.

[7] G. M. Goodwin, "Application of Strain Analysis to Sheet Metal Forming in the Press Shop," *SAE Paper #680093.*

[8] S. P. Keeler and W. A. Backofen, "Plastic Instability and Fracture in Sheet Stretched Over Rigid Punches," *ASM Transactions Quarterly,* vol. 56, pp. 25 - 48, 1963.

[9] C. H. M. Simha, J. Gholipour, A. Bardelcik and M. J. Worswick, "Prediction of Necking in Tubular Hydroforming Using an Extended Stress-Based Forming Limit Curve," *ASME Transactions: Journal of Engineering Materials and Technology,* vol. 129, pp. 36 - 47, 2007.

[10] T. B. Stoughton, "A General Forming Limit Criterion for Sheet Metal Forming," *International Journal of Mechanical Sciences,* vol. 42, pp. 1 - 27, 2000.

[11] J. Wang, T. M. Link and M. J. Merwin, "AHSS Edge Formability in Sheared-Edge Tension," in *International Conference on New Developments in Advanced High-Strength Sheet Steels*, 2008.

[12] X. Chen, M. F. Shi and H.-C. Shih, "AHSS Shear Fracture Predictions Based on a Recently Developed Fracture Criterion," *SAE International Journal of Materials and Manufacturing,* vol. 3, pp. 723-731, 2010.

[13] X. Wu, H. Bahmanpour and K. Schmid, "Characterization of Mechanically Sheared Edges of Dual Phase Steels.," *Journal of Matreials Processing Technology,* vol. 212, pp. 1209 - 1224, 2012.

[14] A. Gurson, "Continuum Theory of Ductile Rupture by Void Nucleation and Growth - Part I: Yield Criteria and Flow Rule for Porous Media," *Journal of Engineering Materials and Technology,* vol. 99, pp. 2 - 15, 1977.

[15] V. Tvergarrd and A. Needleman, "Analysis of Cup-Cone Fracture in a Round Tensile Bar," *Acta Metallurgica,* vol. 32, pp. 157 - 169, 1984.

[16] J. Besson, D. Steglich and W. Brocks, "Modeling of Crack Growth in Round Bars and Plane Strain Specimens," *International Journal of Solids and Structures,* vol. 38, pp. 8529 - 8284, 2001.

[17] L. Xue, "Constitutive Modeling of Void Shearing Effect in Ductile Fracture of Porous Materials," *Engineering Fractrue Mechanics,* vol. 75, pp. 3343 - 3366, 2008.

[18] L. Nahshon and J. Hutchinson, "Modification of the Gurson Model for Shear Failure," *European Journal of Mechanics - A/Solids,* vol. 27, pp. 1 - 17, 2008.

[19] F. Reis, L. Malcher, F. Andrade Pires and J. Cesar de Sa, "A Comparison of Shear Mechanisms for the Prediction of Ductile Failure under Low Stress Triaxiality," *Internatioanl Journal of Structural Integrity,* vol. 1, pp. 314-331, 2010.

[20] C. Butcher, Z. Chen, A. Bardelcik and M. Worswick, "Damage-Based Finite-Element Modeling of Tube Hydroforming," *International Journal of Fracture,* vol. 155, pp. 55 - 65, 2009.

[21] A. Khan and H. Liu, "A New Approach for Ductile Fracture Prediction on Al 2024-T351 Alloy," *International Journal of Plasticity,* vol. 35, pp. 1 - 12, 2012.

[22] G. Johnson and W. Cook, "Fracture Characteristics of Three Metals Subjected to Various Strains, Strain Rates, Temperatures and Pressures," *Engineering Fracture Mechanics,* vol. 21, pp. 31 - 48, 1985.

[23] Y. Bao and T. Wierzbicki, "On Fracture Locus in the Equivalent Srain and Stress Triaxiality Space," *International Journal of Mechanical Sciences,* vol. 46, pp. 81 - 98, 2004.

[24] L. Xue, "Damage Accumulation and Fracture Initiation in Uncracked Ductile Solids Subject to Triaxial Loading," *International Journal of Solids and Structures,* vol. 44, pp. 5163 - 5181, 2007.

[25] Y. Lou, H. Huh, S. Lim and K. Pack, "New Ductile Fracture Criterion for Prediction of Fracture Forming Limit Diagrams of Sheet Metals," *International Journal of Solids and Structures,* vol. 49, pp. 3605 - 3615, 2012.

[26] Y. Lou and H. Huh, "Extension of a Shear-Controlled Ductile Fracture Model Considering the Stress Triaxiality and the Lode Parameter," *International Journal of Solids and Structures,* vol. 50, pp. 447 - 455, 2013.

[27] C. Coulomb, "Essai sur une Application des Regles des Maximis et minimis a Queles Problems de Statitque Relatif a l'Architecture," *Memoire de l'Academie Royal des Science,* 1776.

[28] H. Tresca, "Memoire sur l'Ecoulement des Corps Soumis a de Fortes Pressions," *Comptes Rendus de l'Academie de Science,* vol. 59, pp. 754 - 791, 1864.

[29] T. Wierzbicki, Y. Bao, Y.-W. Lee and Y. Bai, "Calibration and Evaluation of Seven

Fracture Models," *International Journal of Mechanical Sciences,* vol. 47, pp. 719 - 743, 2005.

[30] Y. Bai and T. Wierzbicki, "Application of Extended Mohr-Coulomb Criterion to Ductile Fracture," *International Journal of Fracture,* vol. 161, pp. 1-20, 2010.

[31] D. Mohr and S. Marcadet, "Micromechanically-Motivated Phenomenological Hosford-Coulomb Model for Predicting Ductile Fracture Initiation at Low Stress Triaxialities," *International Journal of Solids and Structures,* Vols. 67 - 68, pp. 40 - 55, 2015.

[32] W. Hosford, "A generalized Isotropic Yield Criterion," *Journal of Applied Mechanics,* vol. 96, pp. 33 - 39, 1972.

[33] Y. Bai and T. Wierzbicki, "A New Model of Metal Plasticity and Fracture with Pressure and Lode Dependence," *International Journal of Plasticity,* vol. 24, pp. 1071-1096, 2008.

[34] K. Kofiani, A. Nonn, T. Wierzbicki, C. Kalwa and C. Walters, "Experiments and Fracture Modeling of High-Strength Pipelines for High and Low Stress Triaxialities," in *Proceedings of the Twenty-Second (2012) International Offshore and Polar Engineering Conference*, Rhodes, 2012.

[35] G. Gruben, E. Fagerholt, O. Hopperstad and T. Borvik, "Fracture Characteristics of a Cold-Rolled Dual-Phase Steel," *European Journal of Mechanics - A/Solids,* vol. 30, pp. 204 - 218, 2011.

[36] T. Wierzbicki, Y. Bao and Y. Bai, "A New Experimental Technique for Constructing a Fracture Envelope of Metals under Multi-Axial Loading," in *SEM Annual Conference and Exposition on Experimental and Applied Mechanics*, Portland, 2005.

[37] D. Mohr and S. Henn, "Calibration of Stress-Triaxiality Dependent Crack Formation Criteria: A New Hybrid Experimental-Numerical Method," *Experimental Mechanics,* vol. 47, pp. 805 - 820, 2007.

[38] M. Dunand and D. Mohr, "Optimized Butterfly Specimen for the Fracture Testing of Sheet Materials under Combined Normal and Shear Loading," *Engineering Fracture Mechanics,* vol. 78, pp. 2919-2934, 2011.

[39] F. Neukamm, M. Feucht and A. Haufe, "Consistent Damage Modelling in the Process Chain of Forming to Crashworthiness Simulations.," in *LS-DYNA Anwenderforum*, 2008.

[40] F. Neukamm, M. Feucht and A. Haufe, "Considering Damage History in Crashworthiness Simulations," in *LS-DYNA Anwenderforum*, 2009.

[41] G. Chen, M. Shi and T. Tyan, "Fracture Modeling of AHSS in Component Crush Tests,"

SAE International Journal of Materials and Manufacturing, vol. 4, pp. 1 - 9, 2011.

[42] M. Basaran, S. Wolkerling, M. Feucht, F. Neukamm and D. Weichert, "An Extension of the GISSMO Damage Model Based on Lode Angle Dependence," in *LS-DYNA Anwenderforum*, 2010.

[43] LSTC, LS-DYNA Materials Manual, 2012.

[44] L. Xue, "Ductile Fracture Modeling - Theory, Experimental Investigation and Numerical Verification," 2007.

[45] A. Bardelcik and M. Worswick, "Straight Tube Hydroforming of Dual Phase (DP780) Steel Tubes with End Feed," in *Proceedings of Numiform 2010*, Korea, 2010.

[46] W. Muschenborn and H.-M. Sonne, "Influence of the Strain Path on the Forming Limts of Sheet Metal," *Arch. Eisenguttenwesen,* vol. 46, pp. 597 - 602, 1975.

[47] W. Lode, "Vershuche Uber den Einfuss der Mittleren Hauptspannung auf das Fliessen der Metalle Eisen, Kupfer und Nickel," *Zeitschrift fur Physik,* Vols. 11 - 12, pp. 913 - 939, 1926.

[48] ASTM International, Annual Book of ASTM Standards: Metals - Mechanical Testing: Elevated and Low Temperature Tests; Metallography, West Conshohocken, PA, 2003.

[49] M. Sutton, J. Yan, V. Tiwari, H. Schreier and J. Orteu, "The Effect of Out-of-Plane Motion on 2D and 3D Digital Image Correlation Measurements," *Optics and Lasers in Engineerng,* vol. 46, pp. 746 - 757, 2008.

[50] Y. Ling, "Uniaxial True Stress-Strain after Necking," *AMP Journal of Technology,* vol. 5, pp. 37-48, 1996.

[51] A. Nasser, A. Yadav, P. Pathak and T. Altan, "Determination of the Flow Stress of Five AHSS Sheet Materials (DP 600, DP 780, DP 780-CR, DP 780-HY and TRIP 780) using the Uniaxial Tensile and the Biaxial Viscous Pressure Bulge (VPB) Tests," *Journal of Materials Processing Technology,* vol. 210, pp. 429 - 436, 2010.

[52] G. Gutshcer, H.-C. Wu, G. Ngaile and T. Altan, "Determination of Flow Stress for Sheet Metal Forming using the Viscous Pressure Bulge (VPB) Test," *Journal of Materials Processing Technology,* vol. 146, pp. 1 - 7, 2004.

[53] P. Bridgman, Studies in Large Plastic Flow and Fracture, Cambridge, Masachusetts: Harvard University Press, 1964.

[54] P. Ludik, "Elemente der Technologischen Mechanik," *Springer Leipzig,* p. 32, 1909.

[55] M. Dunand, Ductile Fracture at Intermediate Stress Triaxialities: Experimental Investigations and Micro-Mechanical Modeling, Massachusetts Institute of Technology, 2013.

[56] A. Abedini, C. Butcher, D. Anderson, M. Worswick and T. Skszek, "Fracture Characterization of Automotive Alloys in Shear Loading," *SAE International Journal of Materials and Manufacturing,* vol. 8, no. 3, pp. 774 - 779, 2015.

[57] J. Peirs, P. Verleysen and J. Degrieck, "Novel Technique for Static and Dynamic Shear Testing of Ti6Al4V," *Experimental Mechanics,* vol. 52, pp. 729 - 741, 2011.

[58] Y. Bao, "Dependence of Fracture Ductility on Thickness," *Thin-Walled Structures,* vol. 42, pp. 1211 - 1230, 2004.

[59] Y. Lou and H. Huh, "Prediction of Ductile Fracture for Advanced High Strength Steel with a New Criterion: Experiments and Simulation," *Journal of Materials Processing Technology,* vol. 213, pp. 1284 - 1302, 2013.

[60] C. Roth and D. Mohr, "Ductile Fracture Experiments with Locally Proportional Loading Histories," *International Journal of Plasticity,* vol. 79, pp. 328 - 354, 2016.

[61] International Standards Organization, "Metallic Materials - Sheet and Strip - Hole Expanding Test 16630:2009".

[62] C. Chiriac, "A Study of the Plastic Deformation of Sheared Edges of Dual Phase 780 Steel," in *SAE 2010 World Congress and Exhibition*, Detroit, 2010.

[63] A. Konieczny and T. Henderson, "On Formability Limitations in Stamping Involving Sheared Edge Stretching," *SAE 2007 Transactions Journal of Materials and Manufacturing - V116-5,* 2007.

[64] N. Pathak, C. Butcher and M. Worswick, "Assessment of Critical Parameters Influencing the Edge Stretchability of AHSS Sheet," *Submitted to the Journal of Materials Engineering and Performance,* 2016.

[65] Y. Lou, C. Lin, T. Clausmeyer, A. Tekkaya and Y. J. Whan, "Modelling fo Ductile Fracture from Shear to Balanced Biaxial Tension for Sheet Metals," *International Journal of Solids and Structures,* vol. 112, pp. 169 - 184, 2017.